

Observations of Nonlinear Internal Wave Run-Up to the Surfzone

GREGORY SINNETT AND FALK FEDDERSEN

Scripps Institution of Oceanography, University of California, San Diego, La Jolla, California

ANDREW J. LUCAS

Scripps Institution of Oceanography, and Mechanical and Aerospace Engineering, University of California, San Diego, La Jolla, California

GENO PAWLAK

Mechanical and Aerospace Engineering, University of California, San Diego, La Jolla, California

ERIC TERRILL

Scripps Institution of Oceanography, University of California, San Diego, La Jolla, California

(Manuscript received 6 October 2017, in final form 19 December 2017)

ABSTRACT

The cross-shore evolution of nonlinear internal waves (NLIWs) from 8-m depth to shore was observed by a dense thermistor array and ADCP. Isotherm oscillations spanned much of the water column at a variety of periods. At times, NLIWs propagated into the surfzone, decreasing temperature by $\approx 1^\circ\text{C}$ in 5 min. When stratification was strong, temperature variability was strong and coherent from 18- to 6-m depth at semi-diurnal and harmonic periods. When stratification weakened, temperature variability decreased and was incoherent between 18- and 6-m depth at all frequencies. At 8-m depth, onshore coherently propagating NLIW events had associated rapid temperature drops (ΔT) up to 1.7°C , front velocity between 1.4 and 7.4 cm s^{-1} , and incidence angles between -5° and 23° . Front position, ΔT , and two-layer equivalent height z_{1W} of four events were tracked upslope until propagation terminated. Front position was quadratic in time, and normalized ΔT and z_{1W} both decreased, collapsing as a linearly decaying function of normalized cross-shore distance. Front speed and deceleration are consistent with two-layer upslope gravity current scalings. During NLIW rundown, near-surface cooling and near-bottom warming at 8-m depth coincide with a critical gradient Richardson number, indicating shear-driven mixing.

1. Introduction

Internal waves (internal isopycnal oscillations) are ubiquitous in the coastal ocean. In coastal regions, nonlinear internal waves (NLIWs) transport and vertically mix sediment, larvae, and nutrients (e.g., Leichter et al. 1996; Pineda 1999; Quaresma et al. 2007; Omand et al. 2011). As an aggregation mechanism, internal waves can generate patches and fronts of swimming

plankters (e.g., Lennert-Cody and Franks 1999; Jaffe et al. 2017). In the nearshore (defined here as depths $h < 20\text{ m}$), NLIWs can drive temperature fluctuations of up to 6°C at tidal and higher frequencies (e.g., Winant 1974; Pineda 1991; Walter et al. 2014). The nearshore semi-diurnal internal tide can transport nutrients onshore (Lucas et al. 2011a,b), which can cause phytoplankton blooms (Omand et al. 2012). Nearshore NLIWs were also correlated with the presence of phosphate and fecal indicator bacteria near the surfzone (Wong et al. 2012). Although important to nearshore ecosystems, the cross-shore transformation of NLIWs in very shallow water, particularly to the surfzone, is poorly understood.

NLIWs that propagate into the nearshore may be either remotely or locally (on the shelf) generated

 Denotes content that is immediately available upon publication as open access.

Corresponding author: G. Sinnett, gsinnett@ucsd.edu

(Nash et al. 2012). On the shelf, NLIW generation and propagation depends on the bathymetric slope (e.g., Garrett and Kunze 2007), background stratification (e.g., Zhang et al. 2015), and barotropic tides (e.g., Shroyer et al. 2011) and can be modified by upwelling and regional-scale circulation (Walter et al. 2016). In analogy to a surface gravity wave surfzone, as internal waves propagate into shallow water on subcritical slopes, they steepen, become highly nonlinear, and dissipate (e.g., Moum et al. 2003; MacKinnon and Gregg 2005), creating an “internal surfzone” (e.g., Thorpe 1999; Bourgault et al. 2008). NLIWs can have both wave and bore-like properties when propagating upslope on the shelf from 120- to 50-m depth (Moum et al. 2007). NLIWs sometimes form highly nonlinear solitons trailing the leading edge of the dissipating internal tidal bore (e.g., Stanton and Ostrovsky 1998; Holloway et al. 1999). Farther onshore, internal wave run-up occurs as an internal bore—sometimes termed a “bolus” (e.g., Bourgault et al. 2008)—in the “internal swashzone,” analogous to surface bores with wave run-up in the swashzone of a beach (Fiedler et al. 2015).

In the nearshore, NLIWs have been observed often as internal bores associated with the internal tide. In Monterey Bay (at $h = 15$ m), sharp temperature drops in the bottom 10 m associated with the M_2 (12-h period) internal tide steepen into a bore front and precede gradual cooling over several hours before temperature quickly recovers amid intensified mixing (Walter et al. 2012). The 12-h evolution of a semidiurnal nonlinear internal bore near Del Mar California was tracked between 60- and 15-m depth (Pineda 1994). In $h \approx 12$ -m depth, internal tidal bores have been related to nutrient and larvae transport (Pineda 1999). Bottom-trapped (cold) bores were observed near Huntington Beach in the Southern California Bight in depths between 20 and 8 m, attributed to breaking semidiurnal internal waves (Nam and Send 2011). An onshore propagating nonlinear internal wave train was observed between 30- and 10-m depth in a strongly stratified estuary that disintegrated into irregularly spaced, short-duration, bottom-trapped bores (Bourgault et al. 2007), which generated turbulence as they dissipated (Richards et al. 2013). Nearshore NLIWs can have significant temporal variation (e.g., Suanda and Barth 2015) associated with multiple angles of incidence and can strongly interact with one another (Davis et al. 2017, manuscript submitted to *Geophys. Res. Lett.*). High-frequency (periods of minutes) NLIW have also been observed to reflect off of steep internal beaches (Bourgault et al. 2011).

The internal surfzone and swashzone have been delineated in laboratory (e.g., Wallace and Wilkinson 1988; Helfrich 1992; Sutherland et al. 2013a) and

numerical studies (e.g., Arthur and Fringer 2014). Laboratory studies of internal bores typically use a layered lock exchange (e.g., Shin et al. 2004; Marino et al. 2005) or motor-driven paddle to create an internal disturbance (e.g., Wallace and Wilkinson 1988; Helfrich 1992), then quantify the speed and shape of the upslope surge of dense water based on layer density differences and total water depth. Analogous to surface wave breaking, conditions affecting the internal wave-breaking regime and subsequent upslope evolution as a bore were found to be a function of an internal Iribarren number Ir (ratio of internal wave steepness to bathymetric slope) or offshore wave frequency and amplitude (Sutherland et al. 2013a; Moore et al. 2016). The Ir also affected the total upslope bore dissipation and eventual transport of tracers (Arthur and Fringer 2016). However, the relationship between NLIW run-up in the ocean and either idealized laboratory or numerical simulations is not clear.

Scripps Beach, the Scripps Institution of Oceanography (SIO) pier (La Jolla, California), and surrounding canyons provide a natural laboratory to study NLIWs in shallow environments. Canyon currents have been linked to internal waves in this (and other) canyon systems (Shepard et al. 1974; Inman et al. 1976). Recent observations in La Jolla Canyon show an active internal wave field at the semidiurnal frequency. Energy flux is up-canyon as internal oscillations transition to higher harmonics (M_4 and above), indicating onshore propagation of a highly nonlinear and evolving internal wave field (Alberty et al. 2017). In 7-m water depth at the end of the SIO pier (this study location), bottom temperature can drop rapidly, 5°C over minutes (Winant 1974; Pineda 1991). With a four-element cross-shore array on the Scripps pier, cold pulses were observed propagating onshore into the surfzone (Sinnott and Feddersen 2014). However, details of internal run-up to the shoreline, variability, and potential impacts to the nearshore are not well observed.

Here, observations are presented from a dense and rapidly sampling instrument array spanning the nearshore from 18-m depth all the way to the shoreline. Analysis is focused on describing the details of internal run-up across the entire internal swashzone and relating these observations to idealized laboratory and numerical simulations. Experimental details are described in section 2, with some of the first time series and spectral observations of NLIW run-up in water depths as shallow as $h = 2$ m in section 3. Observations of individual run-up events are described in section 4 and related to laboratory and numerical studies. Discussion of these results are in section 5 and concluding remarks are in section 6.

2. Experimental details

a. Location and overview

Temperature and current observations at the SIO pier (32.867°N, 117.257°W) were made during fall (29 September to 29 October) 2014, when stratification in the Southern California Bight is strong (Winant and Bratkovich 1981). The SIO pier is 322 m long and extends west-northwest (288°) into water roughly 7.6 m deep. It is ≈ 500 m southeast of Scripps Canyon, the northern arm of the La Jolla canyon system (Fig. 1a). The shoreline is roughly alongshore uniform from 200 m north to 500 m south of the pier, with mean cross-shore slope $s \approx 0.027$ from the shoreline to $h = 18$ -m depth before a steep canyon break. The reference depth ($z = 0$) is at the mean tide level (MTL), and the cross-shore origin ($x = 0$) is defined as the shoreline at MTL. The x coordinate axis is aligned with the length of the pier (positive onshore), making the y axis oriented alongshore (positive toward the north, Fig. 1a). The alongshore origin ($y = 0$) is defined at the northern edge of the pier.

b. Instrumentation

For the 30-day experimental period, a vertical temperature chain was deployed at $h = 18$ m (denoted S18) directly offshore of the pier at $x = -657$ m, $y = 0$ m (green star, Fig. 1a), with 14 Seabird SBE56 thermistors sampling at 2 Hz spaced 1 m apart extending from 1 m above the bed to 3 m below MTL. An additional SBE56 was tethered to a surface float that continually sampled near-surface temperature at a fixed level relative to the tide. Concurrently, 36 Onset Hobo TidBits and 8 Seabird SBE56 thermistors were deployed on the SIO pier pilings ($y = 0$ m) at various cross-shore sites ($-273 < x < -29$ m) and vertical locations ($-5.9 < z < 0.1$ m) (blue and red circles, Fig. 1b). These TidBits and SBE56s sampled water temperature at 3-min and 15-s intervals, respectively, and were calibrated in the SIO Hydraulics Laboratory temperature bath, yielding accuracies of 0.01°C (TidBits) and 0.003°C (SBE56). The TidBits have a 5-min response time and are capable of resolving oscillations at periods longer than 10 min.

A pier-mounted Seabird SBE 16plus SeaCAT maintained by the Southern California Coastal Ocean Observing System (SCCOOS) measured salinity and temperature at $x = -246$ m and $z = -5.8$ m (roughly 1.2 m above the bed), sampling every 6 min (square, Fig. 1b). Salinity was linearly related to temperature over the experiment duration at this site, with salinity of 33.57 ± 0.05 90% of the time. A pier-end Precision Measurement Engineering (PME) vertical temperature chain with 1-m vertical resolution maintained by the SIO Coastal Observing Research and Development

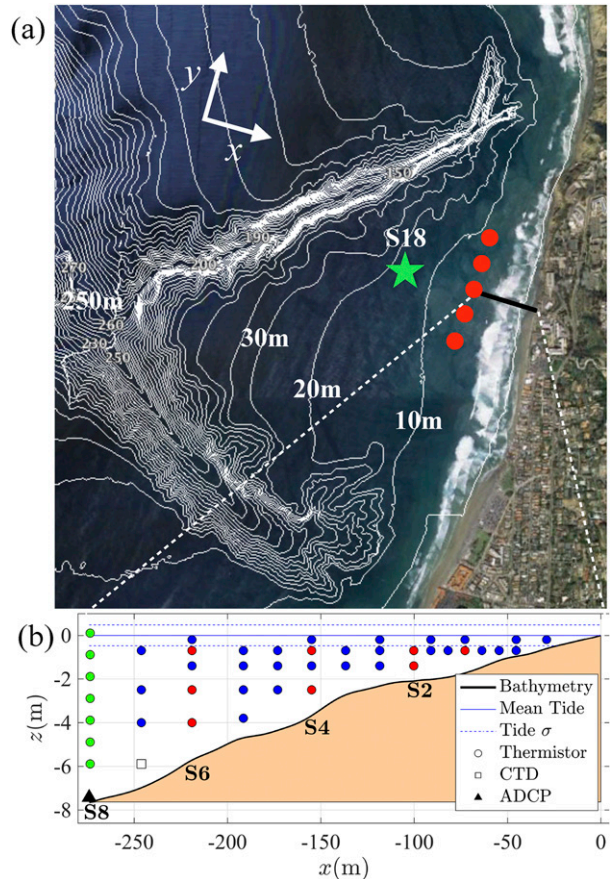


FIG. 1. (a) Google Earth image of the experiment site (La Jolla, CA) and surrounding nearshore waters. The bathymetry (10-m contour interval, white lines) highlights the La Jolla (southern) and Scripps (northern) Canyon system. The site of a moored temperature chain near the 18-m isobath (green star, S18), bottom-mounted thermistors (red dots), and the SIO pier (black line) are shown. The x coordinate is chosen to be along the pier (cross shore). (b) Detail showing the cross-shore (x) instrument deployment locations along the SIO pier (symbols) with reference to the mean tide level $z = 0$ m (blue line), tidal standard deviation (blue dotted), and mean bathymetry (solid black). Three different types of thermistors were deployed: Onset TidBits (blue), SBE56 (red), and the CORDC temperature chain (green). Instrument sites near the 8-, 6-, 4-, and 2-m isobaths are indicated (S8, S6, S4, and S2).

Center (CORDC) provided temperature measurements at 1-Hz sampling rate with 0.01°C accuracy (green circles, Fig. 1b). This temperature chain (installed to examine long-term trends) was offline from 2 to 6 October, and again from 16 to 18 October. Four additional SBE56 thermistors were mounted 0.3 m above the bed in depth $h \approx 7.6$ m at $x = -273$ m and alongshore locations spaced 100 m apart ($y = -200, -100, 100,$ and 200 m; red dots, Fig. 1a). These instruments were active 9–30 October and sampled temperature at 1 Hz to capture alongshore variation and incident event angle relative to

the slope. Temperature data from near-surface pier-mounted thermistors were removed at times when they were exposed to air (low tide or large waves) following [Sinnott and Feddersen \(2014\)](#). For convenience, the pier-mounted instrument site locations near the 8-, 6-, 4-, and 2-m isobaths ($x = -273, -219, -155, \text{ and } -100\text{ m}$) are hereinafter referred to as S8, S6, S4, and S2 (see [Fig. 1b](#)).

Water column velocity was observed by an upward-looking Nortek Aquadopp current profiler deployed in 7.6-m depth at S8 (black triangle, [Fig. 1b](#)). It sampled with 1-min averages and 0.5-m vertical bin size. The ADCP was placed 5 m north of the pier ($y = 5$) to reduce pier-piling flow disturbance, while remaining consistent with pier-mounted thermistors. Velocity data were rotated into the x and y coordinate system based on compass headings taken at deployment. Data above the surface wave trough or in regions with low acoustic return amplitude were removed (≈ 1.5 m below the tidal sea surface).

Meteorological and tide measurements were made by NOAA station 9410230 at S8. Air temperature and wind speed (2-min average) were sampled at $z \approx 18$ m at 6-min intervals. Surface (tidal) elevation η is calculated from an average of 181 one-second samples reported every 6 min. Hourly significant wave height H_s and peak period T_p were observed by the Coastal Data Information Program (CDIP) station 073 (pressure sensor) mounted to a pier piling at S8. When observations were not available (29 September to 21 October), a real-time spectral refraction wave model with very high skill initialized from offshore buoys was used ([O'Reilly and Guza 1991, 1998](#)). Cross-shore bathymetry was measured from the pier deck using lead-line soundings every 10 m on 26 September, 10 October, and 24 October. The bathymetry was then interpolated in x and the time dependent bathymetry was used when appropriate. The average slope between S8 and S4 was $s = 0.033$, with bathymetry variation less than 0.3 m at any location (slope changes $< 4\%$) during the experiment. The outer extent of surface wave breaking (surfzone location x_{sz}) was estimated by shoaling surface wave conditions observed at S8 over the measured bathymetry with the observed tides following [Sinnott and Feddersen \(2016\)](#).

c. Background conditions

The experiment site has a mixed barotropic tide with amplitudes over the 30-day experiment period varying between 0.17 and 1.05 m on a spring-neap cycle, dominated by the lunar semidiurnal (M_2) and lunar diurnal (K_1) tidal constituents ([Fig. 1a](#)). Wind conditions were generally calm, with a light afternoon sea breeze rarely peaking above 5 m s^{-1} ([Fig. 2b](#)). Pier-end (S8) significant

wave height H_s varied from 0.3 to 1.5 m over the entire experimental period. Surface wave events near days 2, 19, 22, and 27 caused significant wave height to peak well above the mean $H_s \approx 0.7$ m. Air temperature followed a strong diurnal heating and cooling cycle in the first 10 days of the record, with diurnal variations $\approx 7^\circ\text{C}$ ([Fig. 2d](#), black). The diurnal air temperature variation decreased to $\approx 4^\circ\text{C}$ after day 10, with a subtle cooling trend seen throughout the record. Surface water temperature (from the S18 surface thermistor) varied weakly, but contained a diurnal heating and cooling signature ([Fig. 2d](#), red). Diurnal air and near-surface ($z > -3.5$ m) water temperature variability was coherent with a ≈ 4 h lag. Diurnal air and water temperature variability below $z = -3.5$ m was incoherent.

3. Month-long nonlinear internal wave observations from 18-m depth to shore

Temperature observations from 18-m depth to near the shoreline at five cross-shore locations ([Figs. 3a–e](#)) highlight the rich and diverse NLIW field present during the 30-day observational period. The first 10 days were strongly stratified at S18 ($x = -657\text{ m}$, $h = 18\text{ m}$) with a large barotropic tide ([Fig. 3e](#)). During this time, winds were typically calm, with a few events where $u_w > 4\text{ m s}^{-1}$. Significant wave height averaged 0.8 m during the first four days, then decreased to less than 0.5 m and remained small until day 19. An energetic NLIW field is present at S18 during the first 10 days, with large vertical isotherm excursions (20°C isotherm displacement is $\pm 6\text{ m}$, [Fig. 3e](#)). At this time, cross-shore coherent cooling events at semidiurnal and faster time scales are regularly observed in the otherwise warm shallow water and can reduce the S4 temperature by 2.25°C in only 10 min. Clear examples of NLIW cross-shore excursions occur near days 1 and 8 ([Fig. 3](#)). The 10-day period containing strong internal wave activity typical of early fall conditions at this site is denoted “period I.”

The early to late fall transition between period I and the less active remaining 20 days (termed “period II”) is characterized by cooling surface water ($z > -7\text{ m}$) and warming at depth ([Fig. 3e](#)). The transition occurs just after day 10, when warm water extended all the way to the bottom at S18 with very weak stratification. At this time, surface gravity waves were weak ($H_s < 0.5\text{ m}$) and sustained winds were moderate ($u_w < 5\text{ m s}^{-1}$) with spring barotropic tides ([Fig. 2](#)). At S18, vertical excursions of the 20°C isotherm were smaller during period II, usually less than $\pm 3\text{ m}$. Near-surface diurnal temperature oscillations due to solar heating were $\pm 0.2^\circ\text{C}$ at S18, increasing to $\pm 0.5^\circ\text{C}$ at S2, and were coherently observed at all cross-shore locations. Though the water was

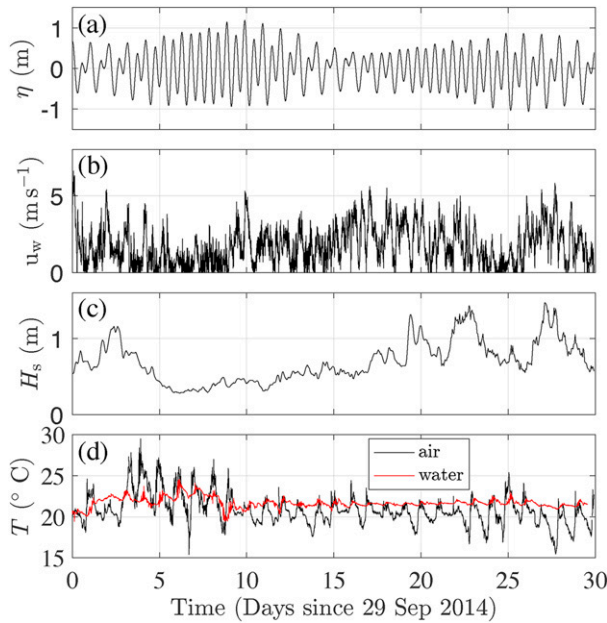


FIG. 2. Observed (a) SIO pier tidal elevation η , (b) wind speed u_w , (c) significant wave height H_s at the SIO pier end (S8), and (d) air (black) and surface ocean in 18-m depth (red) temperature vs time. Wave observations were made by the CDIP station 073. Tidal observations, wind speed, and air temperature were observed by NOAA station 9410230 located at the pier end.

less stratified and isotherm excursions were smaller at S18, NLIW events were still observed during period II (notable in Fig. 3 near days 12 and 27). Cross-shore coherent NLIW events are described in greater detail by zooming in to a time of energetic NLIW activity (identified by the black bar, Fig. 3e) during period I.

The 3.5-day energetic NLIW period (Fig. 4) had strong stratification and barotropic tides but weak winds and surface waves. Temperature variability at all cross-shore locations is strong, containing oscillations at periods near M_2 , the M_4 harmonic (6.2 h period), and higher frequencies. At S18, the $T = 20^\circ\text{C}$ isotherm excursions are over 10 m and NLIW events are coherently observed all the way to S2. Midwater column temperature fluctuations are as high as 4.8°C in 10 min at S18, but decrease onshore with a maximum temperature fluctuation of 2.0°C at S2. The first 1.5 days (days 7–8.5) are strongly stratified with very warm surface water and a sharp thermocline. Near-bottom M_4 temperature variability is present at all cross-shore locations. Stratification is weaker during days 8.5 to 10.5 (Fig. 4), yet temperature variability at all locations is still observed primarily at M_2 periods, although M_4 variability is also present, particularly at S8 (Fig. 4d).

High-frequency temperature variability (periods shorter than 3 h) is superimposed on top of the

M_2 and M_4 variability. The cross-shore evolution of high-frequency variability is visible in a 9-h zoom (Fig. 5) of the time period indicated by the black bar in Fig. 4e. At S18, the $T = 20^\circ\text{C}$ isotherm gradually rises during the first hour with little high-frequency temperature variability. Then, at hour 1.5, the 20°C isotherm plunges roughly 10 m, beginning a series of oscillations at ≈ 10 -min period that persist over the next 6 h (Fig. 5e). The first two 10-m oscillations of the 20°C isotherm near hour 2 are qualitatively similar to a soliton. These superimposed high-frequency oscillations at S8 are present at S6, but decay in shallower water, though some aspects of the high-frequency NLIW field are coherent upslope. For example, near hour 7 at S18 (the peak of the M_4 period event) a pulse of cold water elevates S8 isotherms (lasting roughly 10 min). The cold pulse arrives at progressively later times upslope, until it is finally observed at S2 just before hour 8 (Figs. 5a–d). The pulse propagated onshore at an unknown angle and affected temperature in water depths as shallow as 2 m, causing temperature there to drop 0.7°C in 5 min.

Although occasional pulses of cold water can be tracked coherently upslope, very little high-frequency energy is coherent between S18 and S8. A further zoom of 1.5 h shows temperature with the 18.1° , 19.6° , and 21.1°C isotherms highlighted to emphasize the lack of cross-shore coherence at high frequency (Fig. 6). At S18, isotherms are displaced $\pm 0.8\text{ m}$ at ≈ 10 -min period (Fig. 6e). At S8, isotherm displacements are ± 0.4 , reduced from S18 (Fig. 6d). However, isotherm displacements are not coherent between S18 and S8, with near-zero correlation for all lags during this active 90-min period. A transition to temperature variability on longer time scales and an upslope isotherm tilt is also evident in Fig. 6, as the 90-min average 21.1°C isotherm depth is approximately 2 m higher at S4 than at S18. At S8, both the 19.6° and 21.1°C isotherms contain variability at ≈ 10 -min periods, particularly in the last 40 min (Fig. 6d). Upslope at S6, variability at ≈ 10 -min period is evident near the bottom (19.6°C isotherm), but midwater depths ($z \approx -2\text{ m}$) contain variability at longer time scales (Fig. 6c). The resulting variability of the 21.1°C isotherm at S4 is predominantly at 20-min periods, with less high-frequency variability than in deeper waters (cf. Figs. 6b,d).

The temperature observations (Figs. 3–6) with large-amplitude isotherm displacements relative to water depth, rapid temperature changes, and M_4 harmonics demonstrate the presence of a rich NLIW field. Spectral properties of the NLIW field are explored focusing on the midwater column temperature time series from fast sampling SBE56 thermistors at $z = -9\text{ m}$ at S18, and $z = -4\text{ m}$ at S6 (Figs. 7a,b). During the active

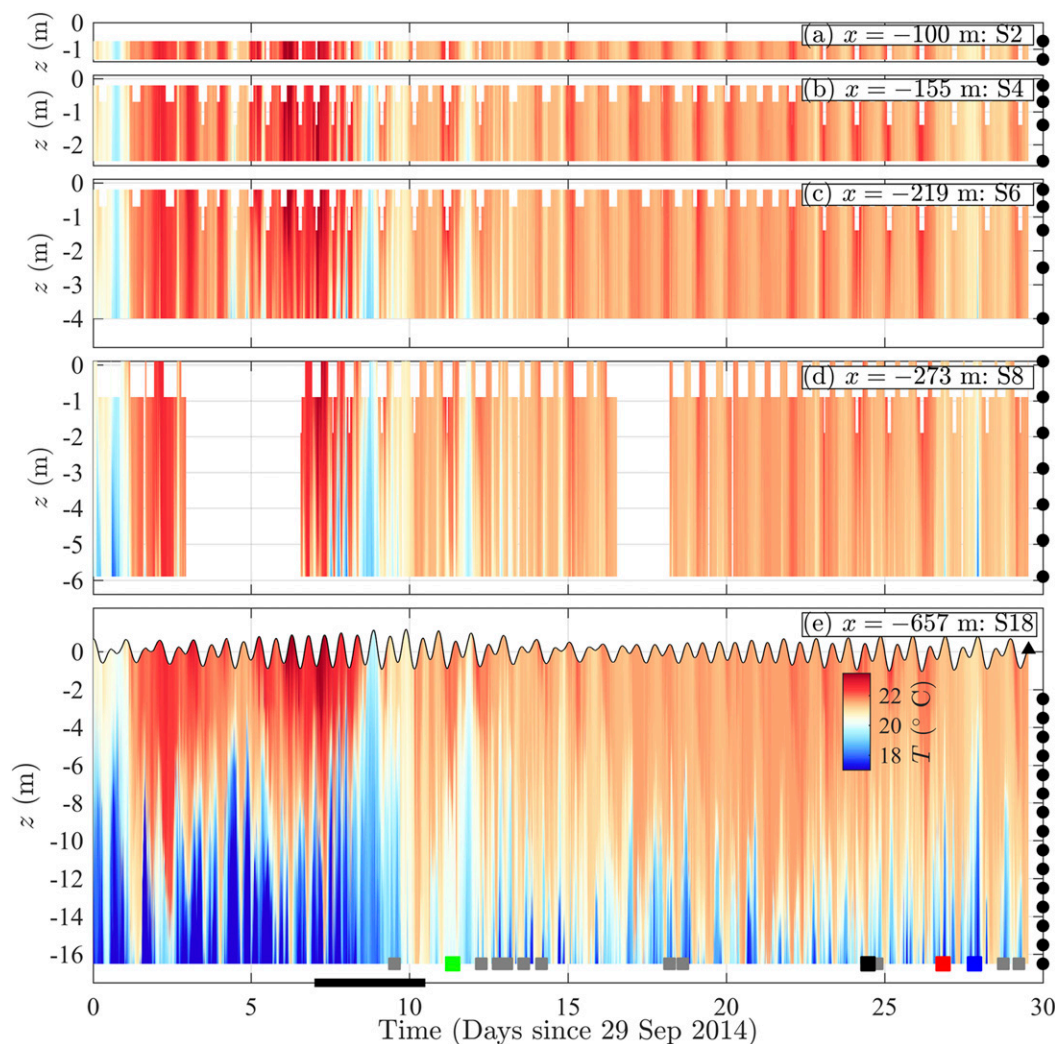


FIG. 3. Temperature vs vertical location below the MTL z and time at cross-shore locations (a) $x = -100$ m, $h \approx 2$ m, denoted S2; (b) $x = -155$ m, $h \approx 4$ m, denoted S4; (c) $x = -219$ m, $h \approx 6$ m, denoted S6; (d) $x = -273$ m, $h \approx 8$ m, denoted S8; and (e) $x = -657$ m, $h \approx 18$ m, denoted S18. The vertical axes have been scaled to approximate the depth at each cross-shore location [the vertical scale of (e) is compressed to fit on the page]. Data in (a)–(d) have been removed (white) when sensors were inoperative or above the water line. Black dots (right side, all panels) indicate the fixed (relative to MTL) thermistor locations. The black triangle in (e) indicates the surface-following sensor (surface level η shown as black line). Gray squares at the bottom of (e) indicate the arrival time of isolated events highlighted in section 4, and colored squares indicate the arrival time of events A–D (left to right), which are highlighted in detail in section 4. The black bar on the abscissa indicates the time span highlighted in Fig. 4.

period I (first 10 days), large (4° – 5°C) temperature oscillations are present at both locations. The less active period II (days 10–30) still has NLIW activity, although the magnitude (1° – 2°C) is much reduced. To contrast these two periods and locations, a 7-day time period is selected to represent period I (red and blue, Figs. 7a,b) and period II (purple and green, Figs. 7a,b). Temperature spectra of these four time series were calculated with the multitaper method (Thomson 1982) using the JLab toolbox (Lilly 2016). The 95% confidence interval

(gray shading) is found from the χ_k^2 distribution with the 14 degrees of freedom given by the orthogonal Slepian tapers.

Period I temperature spectra at S18 (red, Fig. 7c) has peaks at M_2 and M_4 frequencies, and decays with frequency up to a broad secondary peak at 6–10 cph (7–10-min period), corresponding to high-frequency variability at S18 in Fig. 5. Farther upslope, the S6 temperature spectra does not have a clearly defined M_2 peak and the S6 M_2 -band variance is 21% that of S18

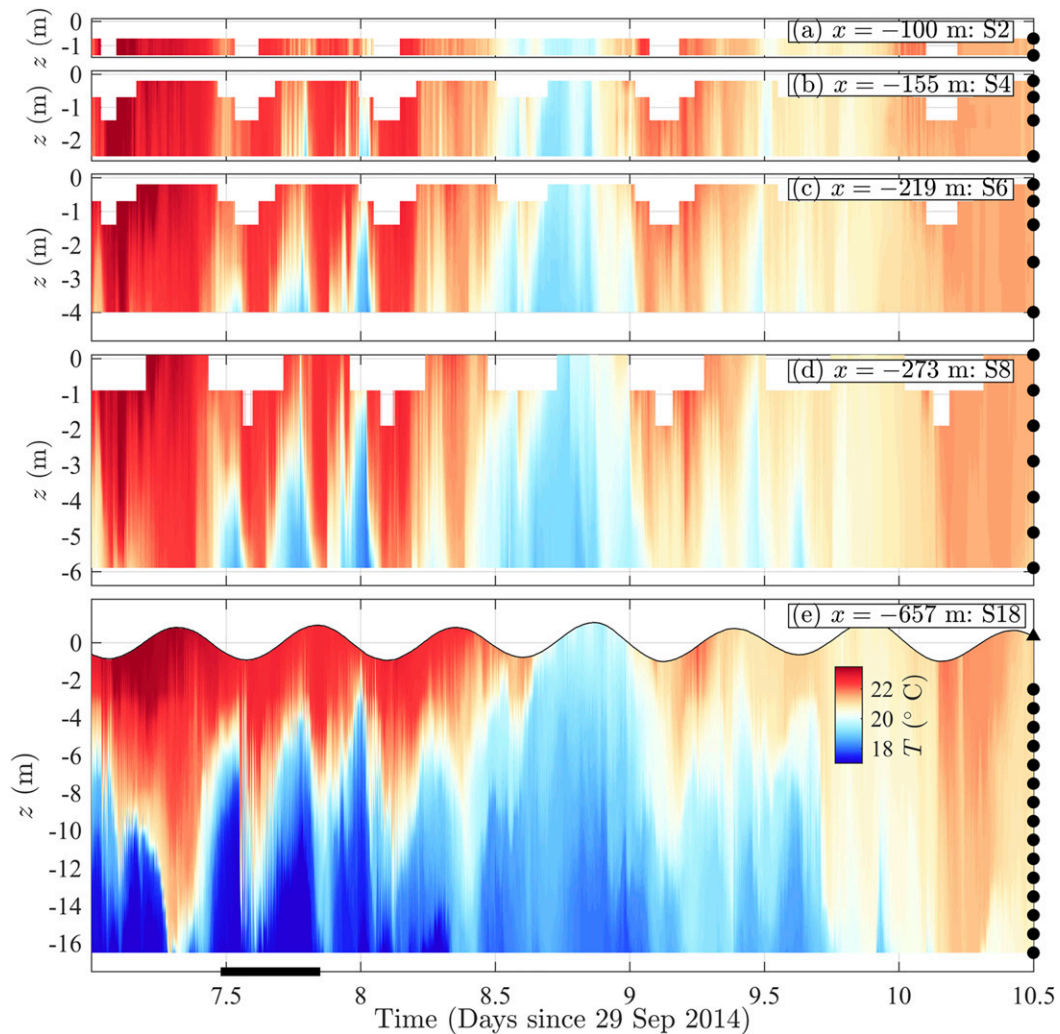


FIG. 4. As in Fig. 3, but with the time axes of all plots zoomed to highlight 3.5 days of internal wave activity. The black bar on the abscissa indicates the timespan included in Fig. 5.

(blue, Fig. 7c). However, at S6 a clear and significant M_4 peak is present that has essentially the same variance as at S18. The M_4 peak indicates either M_2 to M_4 nonlinear energy transfers between S18 and S6 or M_4 generation in deeper water, likely in the offshore canyons (Alberly et al. 2017). An additional small S6 spectral peak is evident near M_8 (harmonic of M_4 , 0.33 cph, 3-h period) with nearly twice as much variance as at S18, suggesting nonlinear energy transfers from M_4 to M_8 between S18 and S6. The S6 spectra falls off similarly to S18, but does not have the broad high-frequency spectral peak, consistent with the reduced onshore high-frequency variability observed in Fig. 5. Between S18 and S6, the M_2 variability was coherent (≈ 0.78 , above the 99% confidence level of 0.39) with 20-min phase lag, suggesting propagation, albeit at an unknown angle. Between S18 and S6, M_4 variability

also was coherent (0.8), as was the M_6 and M_8 variability (at 0.6 and 0.5), albeit more weakly than M_2 and M_4 . However, variability above 1 cph was not coherent between S18 and S6, similar to the zero lagged correlation of the 19.6°C isotherm elevation between S18 and S8 in Fig. 6.

The period II temperature spectra (Fig. 7d) were reduced at all frequencies relative to period I. Spectral peaks at M_2 , M_4 , and higher harmonics are still present at S18 in period II (purple, Fig. 7d), but spectral levels are reduced by a factor of 10 at these frequencies. Furthermore, the period II S18 elevated variability at >1 cph is absent during period II. The period II diurnal temperature variability at S6 (green, Fig. 7d) is slightly elevated relative to S18, consistent with increased solar heating and longwave cooling at the shallower S6 depth, and is coherent between S6 and S18. At M_2 and higher frequencies, the S6 period II

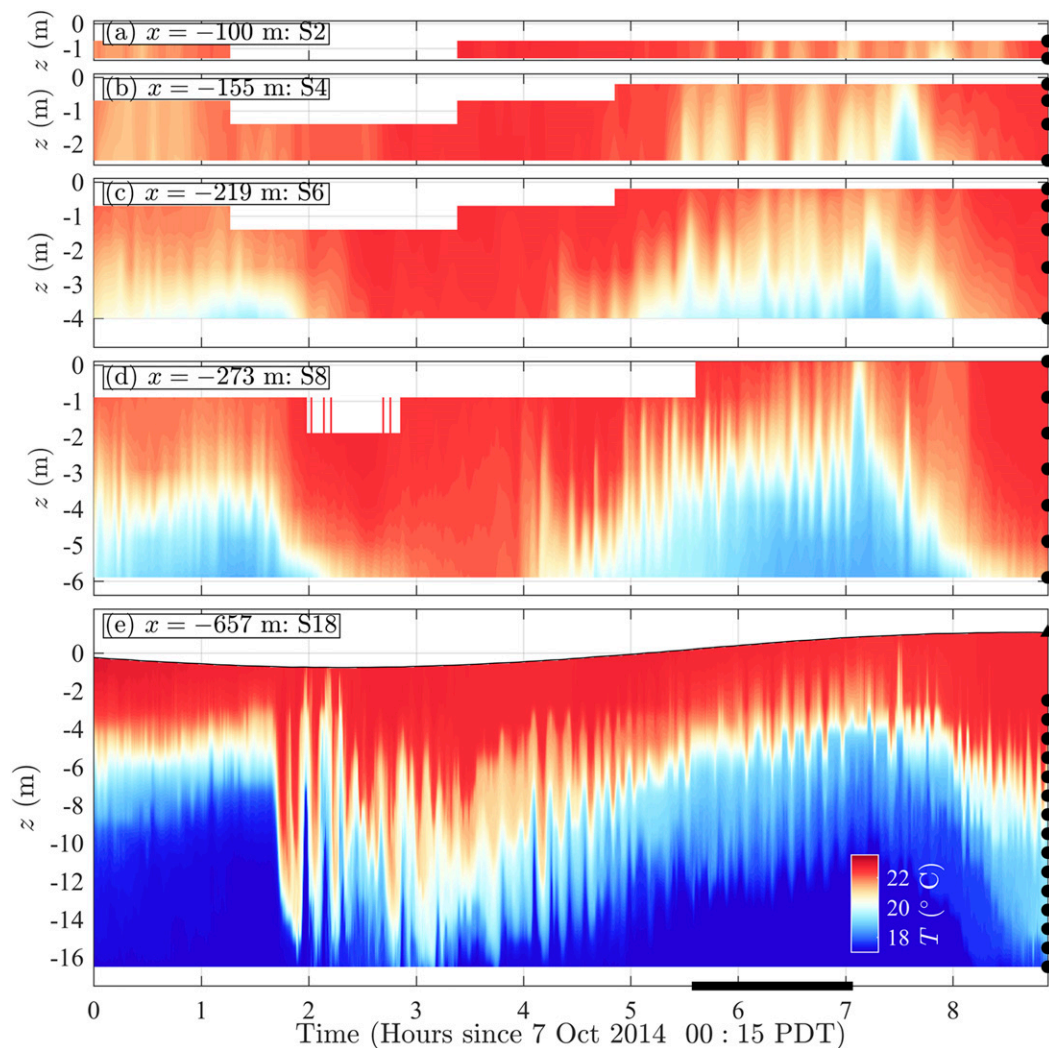


FIG. 5. As in Fig. 4, but with the time axes of all plots zoomed to highlight 9 h beginning on 7 Oct 2014 at 0015 Pacific daylight time (PDT). The black bar on the abscissa indicates the timespan included in Fig. 6

spectra has no significant peaks, was incoherent with S18, and had a total variance half that of S18.

4. Coherent upslope evolution of individual nonlinear internal wave events

The NLIW field observed from S18 (18-m water depth) to near-shoreline S2 (Figs. 3–6) contains cold pulses that propagate coherently upslope (e.g., Fig. 5). The run-up characteristics of these cold pulses ultimately determine the NLIW cross-shore extent and impact to the nearshore region, through, for example, larval transport (e.g., Pineda 1999). Here, the coherent upslope evolution of individual NLIW events is explored in analogy to laboratory studies (e.g., Wallace and Wilkinson 1988; Sutherland et al. 2013a). Events are a significant and rapid reduction and

recovery of temperature near the pier end over a few hours and are defined quantitatively later. Detailed analysis is restricted to between S8 and just seaward of the surfzone at S2, where high thermistor density (Fig. 1b) allowed for coherent upslope tracking of NLIW events. The time period is narrowed to 9–28 October (experiment days 11–30) when the S8 (pier end) alongshore array (red dots, Fig. 1a) was concurrently deployed. A single NLIW event is examined first to introduce important event parameters (e.g., event front speed c_f). Analysis is then broadened to multiple events at S8 and farther onshore, leading to scaling the upslope NLIW event evolution.

a. Example NLIW event characteristics

An example 5-h-long NLIW event occurred on 26 October (red square, experiment day 28, bottom of Fig. 3e)

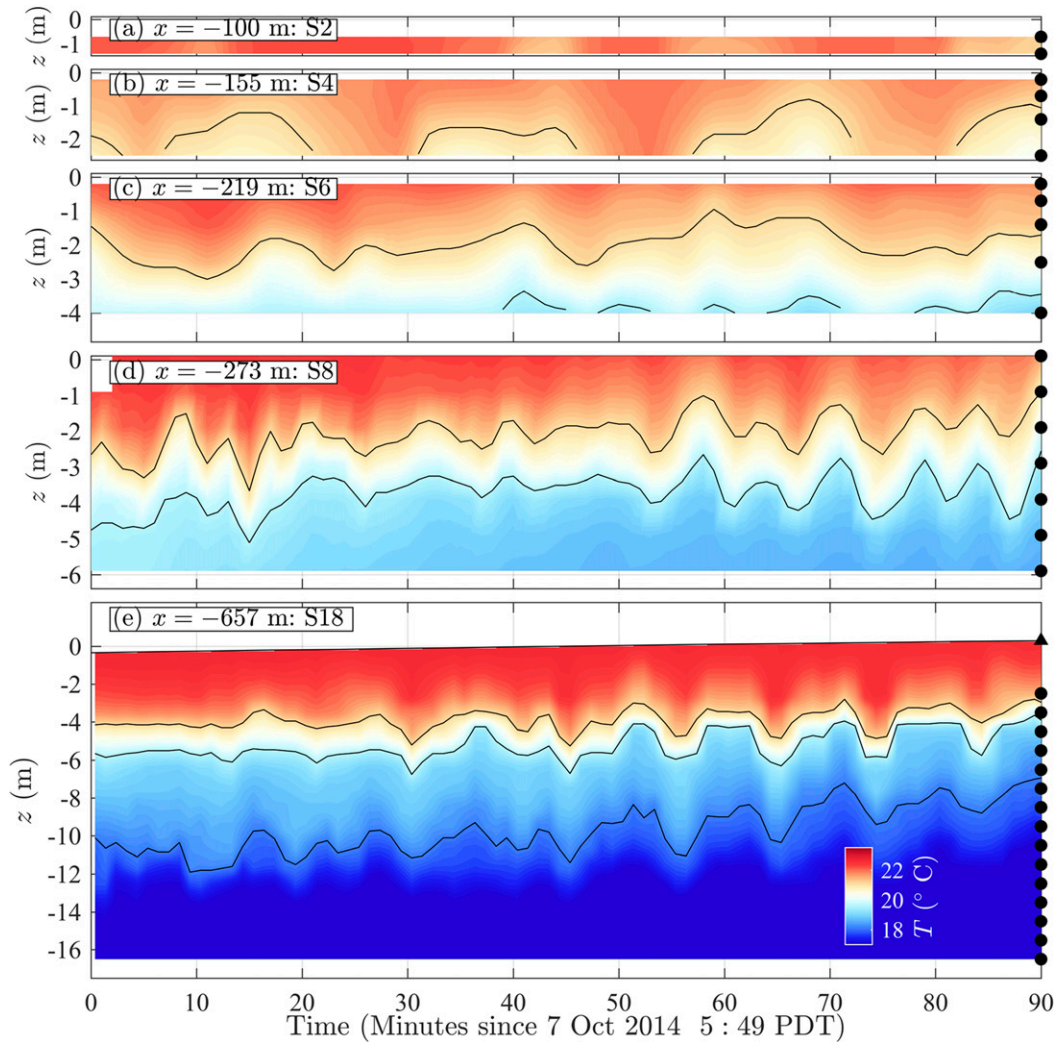


FIG. 6. As in Fig. 5, but with the time axes of all plots zoomed to highlight 1.5 h beginning on 7 Oct 2014 at 0549 PDT. The 18.1°, 19.6°, and 21.1°C isotherms are highlighted with a black curve in all panels.

with large surface wave ($H_s \approx 1.2$ m) and moderate wind ($u_w \approx 3.5$ m s⁻¹) conditions (Fig. 2). This event is selected to highlight NLIW run-up properties. Prior to the event front arrival at hour 1, S8 temperature was essentially constant near 21.2°C and weakly stratified, $dT/dz < 0.01^\circ\text{C m}^{-1}$ (Fig. 8a). After the event front arrival, S8 near-bottom temperature fell rapidly ($\approx 1^\circ\text{C}$ in 1 min) and the water column stratified ($dT/dz < 0.25^\circ\text{C m}^{-1}$). Temperature fluctuations of $O(0.2^\circ\text{C})$ at 1–30-min time scales are observed throughout the water column. Near-bottom temperature began to increase after hour 2 ($\approx 0.025^\circ\text{C min}^{-1}$), while temperature in the upper 3 m cooled slightly. The event concluded between hours 2.75 and 4 as the near-bed warmed and the near-surface cooled until the water column was again weakly stratified near hour 4. During this event, the coldest (bottom)

S8 temperature was near 19.4°C (Fig. 8a), but the coldest (bottom) S18 temperature before the event was near 20.7°C (not shown). Thus, the coldest water at S8 during the event originated from a location deeper than 18 m and traveled horizontally upslope more than 384 m to reach S8.

Velocity associated with the upslope NLIW example event was observed by the ADCP at S8. Cross-shore (U) and alongshore (V) velocities are decomposed into (e.g., for U) depth-averaged (barotropic) velocity \bar{U} and the depth-varying (baroclinic) velocity U' , so that

$$U(z, t) = \bar{U}(t) + U'(z, t), \tag{1}$$

and the vertical average of U' is zero. The barotropic component is assumed to be irrotational in the experiment

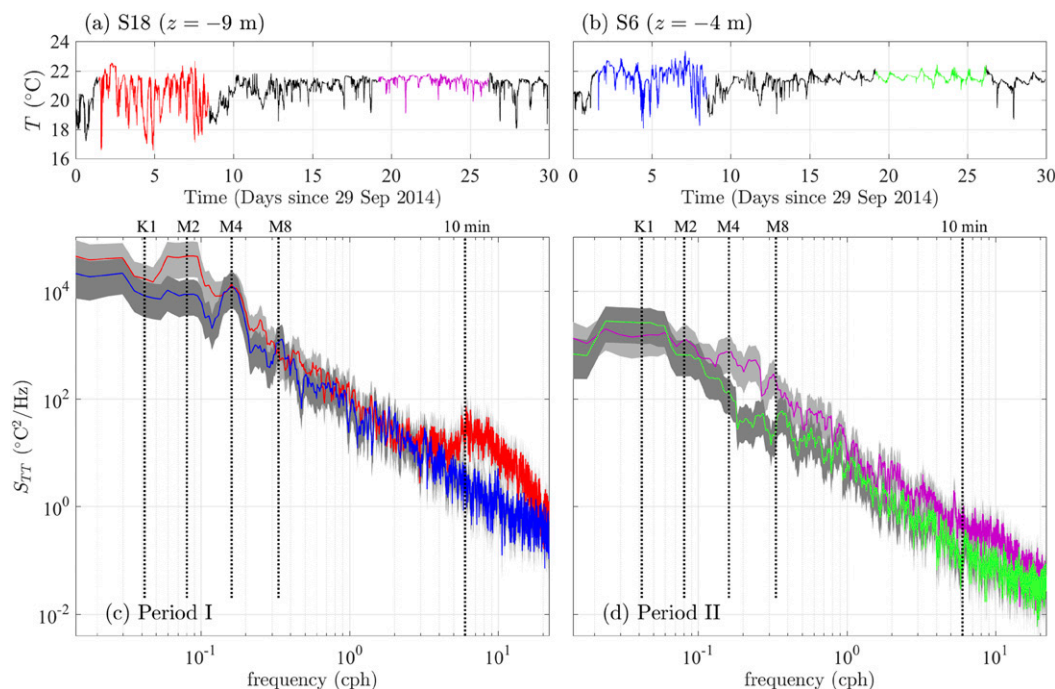


FIG. 7. (top) Midwater column temperature at (a) S18 (green star in Fig. 1) at $z = -9$ m and (b) S6 at $z = -4$ m vs. time. Two 7-day periods containing contrasting internal wave conditions are highlighted at each location. Temperature during days 1.5–8.5 in the active period I is colored red (S18) and blue (S6), and temperature during days 19.2–26.2 in the less active period II is colored purple (S18) and green (S6). (bottom) Temperature spectra vs frequency at both S18 and S6 for (c) period I and (d) period II. Colors correspond to the highlighted periods in (a) and (b), and frequencies corresponding to the 24-h (K_1), 12-h (M_2), 6-h (M_4), 3-h (M_8), and 10-min periods are highlighted (vertical dotted). The 95% confidence interval for spectra at S18 and S6 are shaded light gray and dark gray, respectively.

domain and slowly varying in time. This decomposition is partially aliased by the removal of velocity bins near the tidal sea surface. Prior to the event onset, barotropic velocity magnitude was weak (<0.05 m s⁻¹) as was baroclinic velocity magnitude (almost always $U' < 0.02$ m s⁻¹). However, after the abrupt temperature drop at hour 1 signaling the event arrival (Fig. 8a), baroclinic velocity U' increased, with onshore velocity at depth exceeding 0.06 m s⁻¹ and offshore velocity near the surface (Fig. 8b). The baroclinic current was predominantly in the cross-shore (U') direction, with a weak alongshore (V') component (Fig. 8c). Near hour 2, the direction of U' reverses, and thereafter the near-bed flow is offshore and the near-surface flow is onshore, coincident with the bottom temperature recovery (Figs. 8a,b). During the recovery (2.75–4 h), the transition depth between near-surface cooling and near-bed warming is $z \approx -3$ m (Fig. 8a), which is also near the U' zero crossing depth.

The near-bottom upslope event temperature evolution (Fig. 9) is key to determining event parameters. Prior to the event start at hour 1, the region from S8 to the shoreline was essentially homogeneous in T (Fig. 9a). The pier-end, near-bottom T was also largely uniform in the alongshore (Fig. 9b). At each cross-shore

and alongshore location, the event arrival is clearly visible as a steep drop in T (the event front) that propagates coherently in the alongshore and cross-shore. This T drop then slowly reaches a minimum before beginning to recover near hour 2. At S8, the overall temperature drop of about 2°C was fairly uniform, spanning 400 m in the alongshore (Fig. 9b). In the cross-shore, the temperature drop is coherent and reduced onshore to $x = -137$ m (black curve in Fig. 9a). Onshore of $x = -137$ m, neither a sharp nor coherent temperature drop is observed (dashed curves in Fig. 9a). By hour 4 the event is over and temperature has largely recovered to the pre-event value, albeit with occasional remnants of colder water upslope (e.g., yellow, magenta, and blue curves at hour 4.2 in Fig. 9a).

The example event's upslope near-bottom temperature evolution (Fig. 9) highlights key quantifiable event-front characteristics. The sharp temperature drop indicates the event front arrival time t_{f1} , defined as when the 3-min-averaged temperature change $dT/dt < -0.033$ °C min⁻¹ (gray dots, Fig. 9). Onshore (+ x) NLIW event front propagation is evident from the progression of t_{f1} at different cross-shore locations (Fig. 9a). Similarly, the alongshore event front arrivals

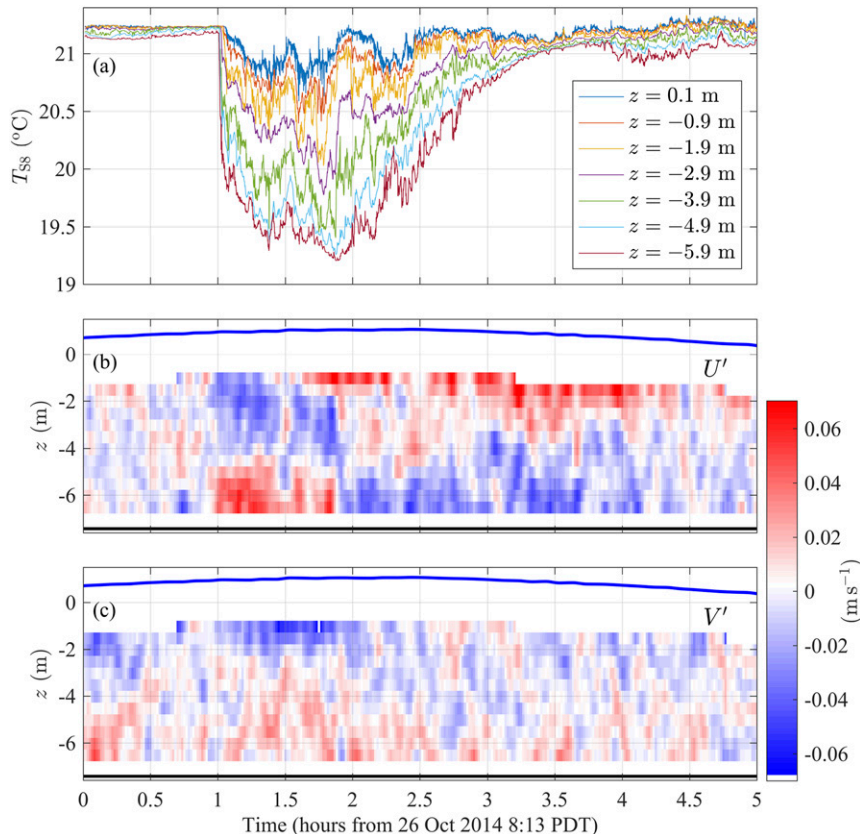


FIG. 8. Five-hour time series of an NLIW run-up event at S8 beginning at 0813 PDT 26 Oct 2014: (a) S8 1-Hz temperature from near surface to near bed, (b) cross-shore baroclinic current U' , and (c) alongshore baroclinic current V' vs depth and time. In (b) and (c), the bed and mean tidal surface are indicated by the black and blue curves, respectively.

(Fig. 9b) indicate a south-to-north (+y) propagation component, consistent with the observed baroclinic velocities (positive near-bottom U' and weakly positive V' at event start; Figs. 8b,c). At a particular cross-shore location, the event front passes at a time t_{f2} , defined as where the 3-min averaged $dT/dt > -0.0067^\circ\text{C min}^{-1}$ (open circles in Fig. 9b). Time t_{f2} does not necessarily correspond to the coldest observed event temperature, but rather to when the sharp event front (rapid T drop) has passed the sensor. The temperature drop ΔT associated with the event front is then defined as

$$\Delta T = T(t_{f1}) - T(t_{f2}). \quad (2)$$

At S8, an event is defined to occur when $\Delta T > 0.3^\circ\text{C}$ over 9 min and is defined to propagate farther upslope (onshore) as long as coherent $\Delta T > 0.15^\circ\text{C}$. For this example event, S8 $\Delta T = 1.26^\circ\text{C}$, but as the event propagated onshore the magnitude of the coherent event front decreased to $\Delta T = 0.34^\circ\text{C}$ at $x = -137$ m (black curve in Fig. 9a). As onshore-coherent $\Delta T > 0.15^\circ\text{C}$ was not observed onshore of $x = -137$ m (dotted

lines, Fig. 9a), the NLIW event run-up cross-shore extent is defined as $x_R = -137$ m.

Event front speed c_f and angle θ are calculated using the cross-shore and alongshore event arrival time and the observed barotropic velocity. The change in event front alongshore arrival position versus time dy_f/dt at S8 is estimated from the slope of the linear fit of alongshore front location y_f versus arrival time when $\Delta T > 0.3^\circ\text{C}$ at three or more alongshore locations. Similarly, the S8 cross-shore change in position versus time, dx_f/dt , is found from the arrival time difference between bottom sensors at S8 ($x = -273$ m) and $x = -246$ m. At S8, the event propagation angle estimated as

$$\theta = \arctan\left(\frac{dx_f/dt}{dy_f/dt}\right), \quad (3)$$

which is independent of the barotropic current. Although barotropic motions do not affect θ , they do affect c_f (in this case by approximately 30%). Accounting for barotropic motions, the event front speed is

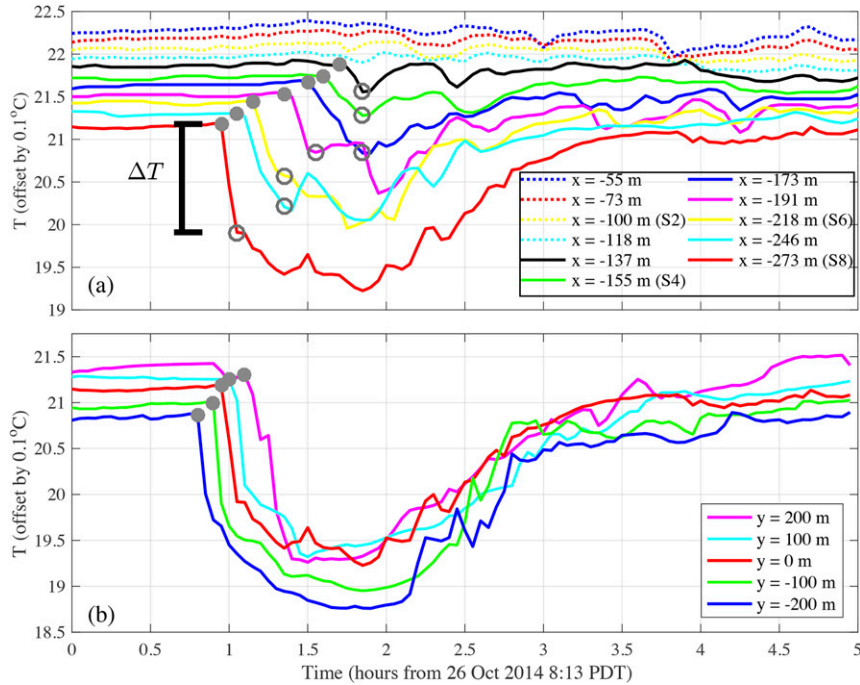


FIG. 9. NLIW event bottom temperature vs time beginning at 0813 PDT 26 Oct 2014 for (a) the cross-shore locations and (b) the pier-end (S8) alongshore locations (red dots in Fig. 1a), offset by 0.1°C in both (a) and (b) for visibility. Gray dots indicate the event arrival time at all locations. Open circles in (a) indicate the temperature change that defines ΔT , with S8 $\Delta T = 1.26^\circ\text{C}$ highlighted. The NLIW event ΔT was below the 0.15°C cutoff threshold onshore of the run-up extent $x_R = -137\text{ m}$, indicated by the dotted lines in (a).

$$c_f = dx_f/dt \cos\theta - \bar{U} \cos\theta - \bar{V} \sin\theta. \quad (4)$$

For this example event, S8 front speed is $c_f = 0.06\text{ m s}^{-1}$ and incidence angle is $\theta = 11.2^\circ$.

Observations of ΔT and c_f can be related to idealized two-layer laboratory and numerical studies of NLIW run-up with defined layer height h_i and layer density difference $\Delta\rho$ (e.g., Sutherland et al. 2013a; Arthur and Fringer 2014). Here, the continuously stratified ocean is related to an idealized equivalent two-layer fluid with layer density difference $\Delta\rho = \alpha\Delta T$ (where α is the coefficient of thermal expansion) and the equivalent two-layer interface height set by equating the change in vertically integrated baroclinic potential energy PE associated with the continuously stratified event front to the potential energy change of a two-layer system with $\Delta\rho$ and layer depth h_i . The instantaneous vertically integrated baroclinic potential energy is

$$\text{PE}(t) = \int_0^{\tilde{h}} [\rho(z', t) - \rho_0] g z' dz', \quad (5)$$

where ρ_0 is a constant reference density, g is gravity, the tidally varying water depth is $\tilde{h} = h + \eta$, and z' is a

vertical coordinate referenced to the bed. The change in PE associated with the event front is

$$\Delta\text{PE} = \text{PE}(t_{f2}) - \text{PE}(t_{f1}). \quad (6)$$

For a two-layer system, the equivalent vertically integrated change in potential energy from t_{f1} to t_{f2} is

$$\Delta\text{PE} = \Delta\rho g (z_{\text{IW}}^2/2), \quad (7)$$

where z_{IW} approximates h_i and is the equivalent two-layer interface height above the bed for the stratified event. Rearranging (7) gives z_{IW} as a function of ΔPE and $\Delta\rho$,

$$z_{\text{IW}} = \left(\frac{2\Delta\text{PE}}{\Delta\rho g} \right)^{1/2}. \quad (8)$$

The two-layer equivalent interface height is then found from (8) using the change in PE due to the event front in the continuously stratified ocean [(6)] and $\Delta\rho = \alpha\Delta T$. For the example event, the S8 interface height is $z_{\text{IW}} = 2.48\text{ m}$, consistent with the large temperature drop in the bottom 2 m and weaker drop at shallower depths. Estimation of z_{IW} depends on adequate vertical temperature

resolution, restricting z_{IW} calculation to cross-shore locations with at least four thermistors in the vertical (Fig. 1b). Having defined key parameters associated with the NLIW event front (ΔT , c_f , z_{IW} , and x_R), the observed range and upslope (onshore) evolution of individual events are investigated next.

b. Individual NLIW event characteristics

Isolated individual NLIW events are defined when $\Delta T > 0.3^\circ\text{C}$ at S8 and when no other cold pulses occur for ± 3 h. This second criterion removes overlapping events (discussed later). With these criteria, a total of 14 individual NLIW events with $0.3^\circ\text{C} < \Delta T < 1.7^\circ\text{C}$ were isolated at the pier end (S8) between 9 and 30 October. Two events had $\Delta T > 1.5^\circ\text{C}$, six events had $1.0^\circ\text{C} < \Delta T < 1.5^\circ\text{C}$, three events had $0.5^\circ\text{C} < \Delta T < 1.0^\circ\text{C}$, and three events had $0.3^\circ\text{C} < \Delta T < 0.5^\circ\text{C}$ (left column, Fig. 10). All 14 events were observed coherently propagating upslope with reduced ΔT so that 54 m farther onshore (at S6) only 10 events were observed, all with $\Delta T > 0.3^\circ\text{C}$ (second column, Fig. 10). Despite the onshore reduction in ΔT , six events (associated with the largest ΔT at S8) were still observed at S4 (right column, Fig. 10). Farther upslope ΔT continued to decrease, but at S2 no coherent $\Delta T > 0.15^\circ\text{C}$ was observed.

At S8, the 14 events propagated upslope with speeds $1.4 < c_f < 7.4 \text{ cm s}^{-1}$ (radial magnitude, Fig. 11a). These NLIW events also propagated with a range of incidence angles ($-5^\circ < \theta < 23^\circ$, Fig. 11a), potentially due to the many internal wave generation locations nearby. The slight positive mean $\theta \approx 5^\circ$, indicates a south-to-north NLIW propagation tendency, suggesting a possible dominant source near the southern La Jolla Canyon (Fig. 1a) through mechanisms described in Albery et al. (2017). During the example event (Fig. 8), the inferred large upslope transport of cold water suggests the event is strongly nonlinear. At S8, event nonlinearity is quantified with the ratio of near-bed baroclinic velocity magnitude $|U'_b|$ to front speed c_f ($|U'_b|/c_f$), where $|U'_b|$ is averaged for 10 min between 0.9 and 1.9 m above the bottom after event onset. For linear internal waves, $|U'_b|/c_f \ll 1$. At S8, the example event detailed in section 4a has $|U'_b|/c_f = 0.7$, indicating strong nonlinearity. The 14 isolated NLIW events had $|U'_b|/c_f$ between 0.3 and 2.0 with a mean value of 0.7.

For these 14 NLIW events, the observed S8 c_f is compared to two-layer gravity current speeds (e.g., Sutherland et al. 2013a; Marleau et al. 2014). A flat-bottom, two-layer fluid with interface height h_i in depth h and upper- and lower-layer densities ρ_0 and $\rho_0 + \Delta\rho$, respectively, has reduced gravity $g' = g(\Delta\rho)/\rho_0$. The

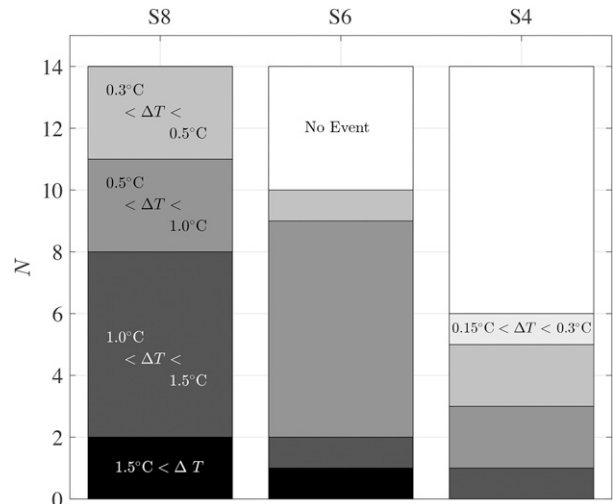


FIG. 10. Number (N) and ΔT distribution (shading) of NLIW events observed between 9 and 30 Oct 2014 at cross-shore locations S8, S6, and S4 (highlighted in Fig. 1b). Of the $N = 14$ events observed at S8, only six were observed at S4, and none with $\Delta T > 1.5^\circ\text{C}$.

corresponding gravity current Froude number is (Shin et al. 2004)

$$F_0 = \sqrt{\delta(1 - \delta)}, \tag{9}$$

where $\delta = h_i/h$. The speed of the gravity current front is

$$c_{gc} = F_0(g'h)^{1/2} = [(1 - \delta)g'h_i]^{1/2} \approx \left[\left(1 - \frac{z_{IW}}{h} \right) g'z_{IW} \right]^{1/2}, \tag{10}$$

where, for a NLIW event, z_{IW} is used for the lower-layer height, \bar{h} is the tidally adjusted water depth, and $\Delta\rho$ is given by $\alpha\Delta T$.

For these 14 NLIW events, the observed S8 upslope event front speed c_f is reasonably well predicted by the two-layer gravity current speed c_{gc} [(10)] with root-mean-square error (RMSE) of 0.016 m s^{-1} , squared correlation $R^2 = 0.44$, and best-fit slope of 1.15 (Fig. 11b). Although c_{gc} is biased high relative to c_f , this bias could be accounted for by adjusting the F_0 definition [(9)]. The reasonably good relationship between c_f and c_{gc} indicates that these continuously stratified NLIW events (e.g., Fig. 8) are reasonably well scaled as a two-layer gravity current (e.g., Shin et al. 2004), even though the events propagate at nonzero incidence angles, the bottom slopes weakly, and the event may be propagating into inhomogeneous (stratified) water.

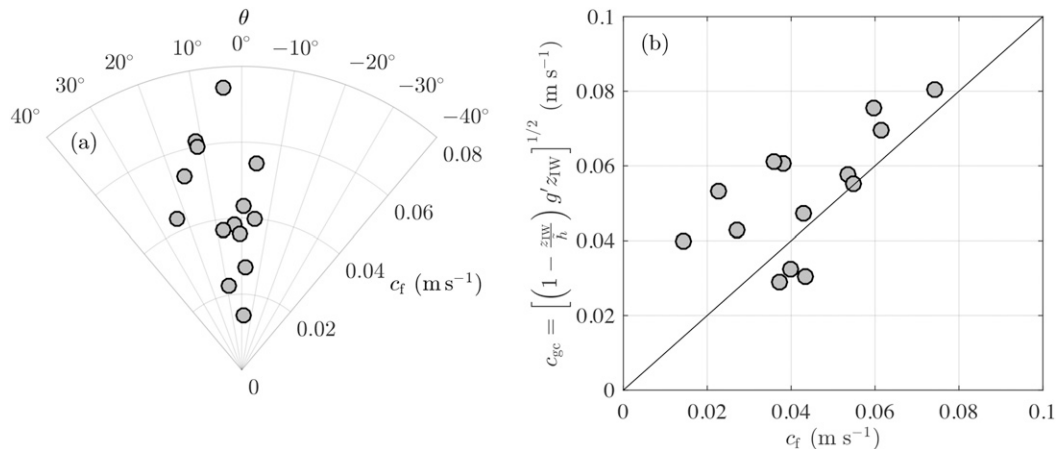


FIG. 11. (a) NLIW event front speed c_f (radial direction) and incident angle θ at S8 for the 14 observed events between 9 and 30 Oct 2014. Events are plotted as if a viewer were looking offshore from the end of the SIO pier. (b) NLIW two-layer gravity current front speed c_{gc} [(10)] vs event front speed c_f [(4)] for the 14 NLIW events observed at S8. The RMSE is 0.016 m s^{-1} , squared correlation R^2 is 0.44, and the best-fit slope is 1.15.

Not all NLIW occurrences are as simple as the example event (Figs. 8, 9) with its clearly defined parameters (e.g., t_{f1} , ΔT , and z_{IW}). NLIW run-up can be complicated, with overlapping cold pulses containing differing c_f and θ (Fig. 12). A near-simultaneous initial cold pulse arrival at S8 alongshore locations (gray dots, Fig. 12b) indicates an NLIW pulse with $\theta = 2.2^\circ$ that propagates onshore (subsequent gray dots, Fig. 12a). A second cold pulse is observed roughly 1.2 h later at S8 cross-shore and alongshore stations (gray crosses, Figs. 12a,b) superimposed on the first pulse. The second pulse was observed within the surfzone (at this time surfzone wave breaking begins at $h = 2 \text{ m}$) and propagated south to north at very high angle and with ΔT decreasing in the alongshore ($\Delta T = 1.08^\circ\text{C}$ at $y = -200 \text{ m}$ but $\Delta T = 0.17^\circ\text{C}$ at $y = 200 \text{ m}$). Though the onset of the second pulse is cross-shore coherent, the temperature drop was observed nearly simultaneously at $x = -55 \text{ m}$, $y = 0 \text{ m}$ and $x = -273 \text{ m}$, $y = -200 \text{ m}$ (gray crosses in Fig. 12a) before giving a sense of rapid offshore propagation as temperature recovered between hours 3 and 4. Although speculative, this pulse may have swept cold water into the surfzone at $y < 0 \text{ m}$ that was then reflected offshore. The second cold pulse propagated through the previously conditioned stratification and current. The criterion requiring isolated events removes such complicated overlapping cases (Fig. 12) where event parameters are difficult to isolate.

c. Upslope NLIW evolution

At S8, 14 isolated NLIW events have $\Delta T > 0.3^\circ\text{C}$ with no overlapping cold pulses. To compare these NLIW events with idealized two-layer laboratory and modeling

studies, the event propagation angle is restricted to be nearly shore normal ($|\theta| < 15^\circ$, eliminating two events). A further restriction requires the wavefront to be roughly alongshore uniform, where ΔT is within 0.5°C at four or more alongshore locations (eliminating eight more events). Background barotropic velocity was weak during each event ($|\bar{U}| < 1.3 \text{ cm s}^{-1}$). These restrictions result in four remaining events (colored markers in Fig. 3e), denoted events A–D, that are near normally incident and propagate into homogeneous conditions. Thus, these representative events are more consistent with a two-layer assumption than the total 14 isolated NLIW events at S8. To relate to laboratory two-layer internal run-up and gravity current studies, these four events are further required to propagate into homogeneous T at and onshore of an initial cross-shore location x_0 . Events B and C had homogeneous T at and onshore of S8 prior to the event, and thus the initial cross-shore location $x_0 = x_{S8} = -273 \text{ m}$. Events A and D had some vertical stratification at S8 prior to the event start. However, just 27 m onshore T was vertically and onshore homogeneous, so $x_0 = -246 \text{ m}$ for events A and D to ensure pre-event homogeneous conditions. Note that the example event in Figs. 8 and 9 is event C. The upslope (onshore) evolution of events A–D (colored dots, Fig. 3e) are explored in detail to highlight NLIW run-up characteristics.

The onshore propagation distance from x_0 is $\Delta x = x - x_0$, and elapsed time from front arrival at x_0 is $\Delta t = t - t_{f1}(x_0)$. Event A–D fronts propagated onshore and slowed down until reaching their eventual total run-up distance $\Delta x_R = x_R - x_0$ (dots, Fig. 13). The upslope transit time was between 42 and 64 min, with Δx_R varying between

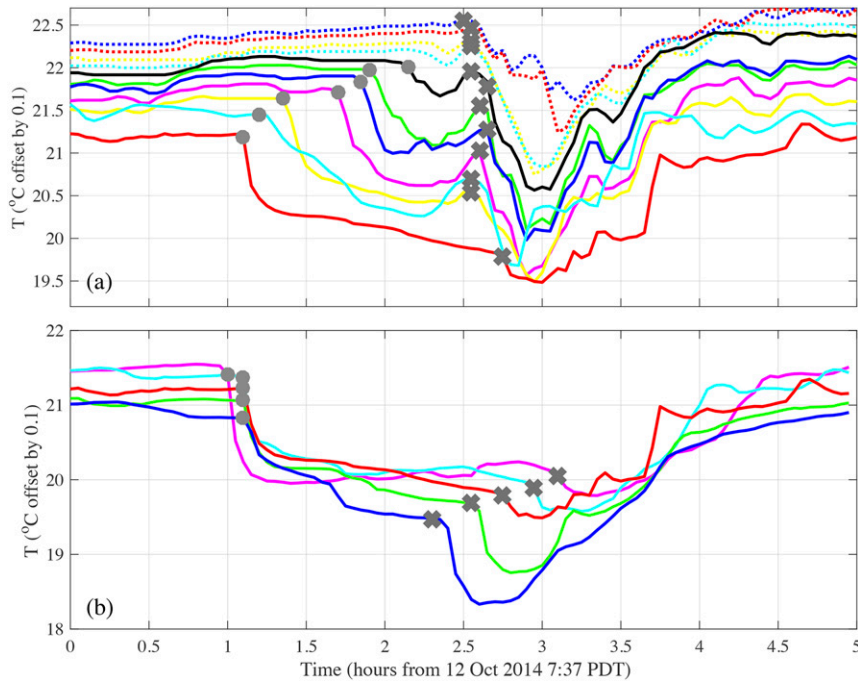


FIG. 12. Bottom temperature vs time beginning at 0737 12 Oct 2014 for (a) cross-shore and (b) alongshore locations (as in Fig. 9) offset by 0.1°C for visibility. Gray dots indicate the arrival of an NLIW cold pulse propagating with nearly zero angle onshore to $x_R = -137$ m. Gray crosses indicate a second NLIW pulse superimposed on the first, propagating at a high angle from south to north. The first NLIW event ΔT was below the 0.15°C cutoff threshold onshore of the run-up extent $x_R = -137$ m, indicated by the dotted lines in (a), though the second pulse caused significant ($\approx 0.8^\circ\text{C}$) temperature reduction in water as shallow as 1 m ($x = -55$ m).

100 and 137 m. The two-layer gravity current speed [(10)] can be expressed as dx/dt , and the differential equation can be solved for change in cross-shore position x , assuming a constant Froude number [(9)] and a constantly sloping bottom. The solution is a quadratic relationship between Δx and Δt , consistent with laboratory observations of broken internal solitary wave upslope run-up (e.g., Sutherland et al. 2013a). So, for each event, the front position Δx and elapsed time Δt are fit to a quadratic

$$\Delta x = -\frac{d_f}{2}(\Delta t)^2 + c_{f0}\Delta t, \quad (11)$$

with best-fit NLIW front speed at x_0 (c_{f0}) and constant onshore NLIW deceleration d_f . The fits all have high skill (>0.98 , lines Fig. 13) with standard error in best-fit parameters found from standard methods (e.g., Wunsch 1996). The NLIW deceleration d_f varies between $(0.9\text{--}2.4) \times 10^{-5} \text{ m s}^{-2}$ with standard error around $0.37 \times 10^{-5} \text{ m s}^{-2}$ (Table 1). Event D had the highest c_{f0} ($7.84 \pm 0.6 \text{ cm s}^{-1}$), but also had the largest deceleration, limiting the run-up distance from x_0 , $\Delta x_R = x_R - x_0$ to 128 m (blue, Fig. 13). Event

A decelerated less than event D, but had a smaller c_{f0} ($5.86 \pm 0.4 \text{ cm s}^{-1}$) resulting in a similar Δx_R . Event C had high c_{f0} ($6.31 \pm 0.6 \text{ cm s}^{-1}$) and also less

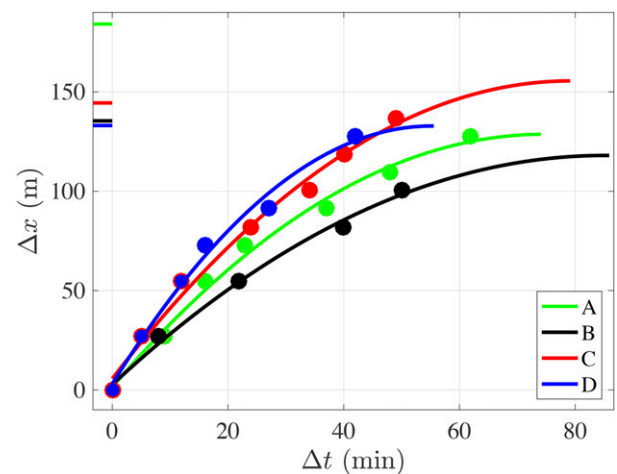


FIG. 13. NLIW event A–D front propagation distance Δx vs elapsed time Δt (colored dots) and quadratic fit (curves) as in (11). There is good agreement (squared correlation >0.98) between the quadratic fit and observations. For each event, the estimated surfzone boundary location $x_{sz} - x_0$ is indicated as a bar on the ordinate.

TABLE 1. Summary of example events A–D detailed in section 4. From left to right: event designator, S8 significant wave height H_s , wind speed u_w , observed event front cross-shore propagation speed c_f , ratio of bottom baroclinic current to event propagation speed $|U'_b|/c_f$, propagation angle θ , event front temperature difference ΔT_0 , equivalent two-layer height z_{IW_0} , best-fit deceleration d_f and standard error, and total run-up distance from x_0 , Δx_R .

Event	H_s (m)	u_w (m s^{-1})	c_f (cm s^{-1})	$ U'_b /c_f$	θ ($^\circ$)	ΔT_0 ($^\circ\text{C}$)	z_{IW_0} (m)	$d_f (\times 10^{-5} \text{ m s}^{-2})$	Δx_R (m)
A	0.32	1.02	3.8	0.8	2.9	1.29	2.32	1.3 ± 0.2	128
B	0.69	0.48	3.6	1.2	1.0	0.96	2.10	0.9 ± 0.4	100
C	1.20	3.36	6.0	0.7	11.2	1.26	2.48	1.3 ± 0.4	137
D	1.03	2.49	7.4	0.4	3.6	1.62	2.12	2.4 ± 0.5	128

deceleration than event D, allowing $\Delta x_R = 137$ m (red, Fig. 13). Event B had the lowest c_{f0} ($4.51 \pm 0.6 \text{ cm s}^{-1}$) and deceleration, with observed $\Delta x_R = 100$ m.

None of these four events were observed to propagate coherently into the surfzone (tick marks along ordinate axis in Fig. 13). During event A, the significant wave height was very small ($H_s = 0.32$ m, Table 1) and the surfzone was narrow. The event run-up halted 56 m offshore of the estimated surfzone boundary (green tick mark, Fig. 13). Event B with $H_s = 0.69$ m also halted more than 35 m from the estimated surfzone boundary. Events C and D had $H_s > 1$ m (Table 1) and with the wider surfzone, the total run-up distance Δx_R was observed to within 10 m of the estimated surfzone boundary. Events C and D both caused thermistors inside the surfzone to cool $\approx 0.1^\circ\text{C}$ in 6 min, though this cooling was insufficient to coherently track further onshore as an event ΔT .

NLIW event front temperature drop ΔT and equivalent two-layer height z_{IW} generally decreases farther upslope (Figs. 14a,b). For events A–D, ΔT at x_0 (ΔT_0) varied between 0.96° and 1.62°C (Fig. 14a), a factor of 1.7. Upslope ΔT decreases differently among events, either rapidly (event B, black in Fig. 14a) or slowly (event A, green). For events B–D, $\Delta T < 0.41^\circ\text{C}$ at x_R . In contrast, the slowly decaying event A had $\Delta T = 0.96^\circ\text{C}$ at x_R . Yet, for event A, no significant temperature drop was present 20 m onshore of x_R . The z_{IW} at x_0 (z_{IW_0}) varied between 2.1 and 2.5 m (Fig. 14b), a much smaller range than for ΔT_0 . Upslope from x_0 , z_{IW} reduced linearly in a relatively similar manner for all events, in contrast to ΔT . At x_R , z_{IW} ranges between 1 and 1.5 m, still significant compared to z_{IW_0} . For events A–D, the upslope reduction in dimensional c_f , z_{IW} , and ΔT and the constant deceleration are qualitatively consistent with laboratory observations of internal run-up of broken internal solitary waves (Wallace and Wilkinson 1988; Helfrich 1992; Sutherland et al. 2013a).

d. Scaling upslope NLIW evolution

The stratified NLIW events A–D have baroclinic velocity structure and temperature structure that are

qualitatively consistent with an upslope two-layer gravity current (e.g., Figs. 8, 9). Events A–D have $|U'_b|/c_f$ that is $O(1)$ (Table 1), also consistent with a gravity current. NLIW events A–D have constant deceleration (Fig. 13) and their density anomaly ΔT and height z_{IW} are reduced onshore consistent with upslope two-layer gravity currents (Marleau et al. 2014). Here, the NLIW event parameters (c_{f0} , d_f , Δx_R , ΔT , and z_{IW}) are scaled and compared to gravity current scalings.

The nondimensional $\Delta T/\Delta T_0$ and z_{IW}/z_{IW_0} dependence upon nondimensional run-up distance $\Delta x/\Delta x_R$ is examined in analogy with laboratory studies of the

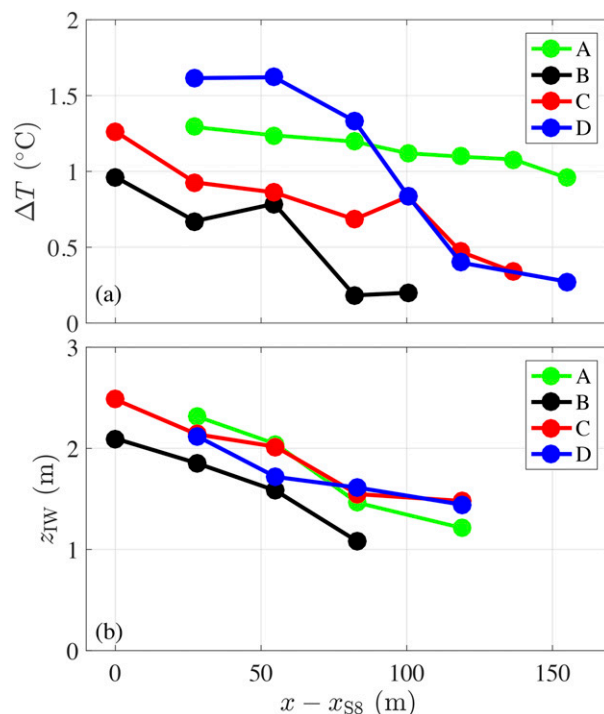


FIG. 14. NLIW events A–D (colored) (a) ΔT and (b) equivalent two-layer interface amplitude z_{IW} vs upslope distance relative to S8 ($x - x_{S8}$). Note that z_{IW} is only estimated at locations with at least four thermistors in the vertical. Events A and D are first estimated at $x - x_{S8} = 27$ m as S8 was prestratified.

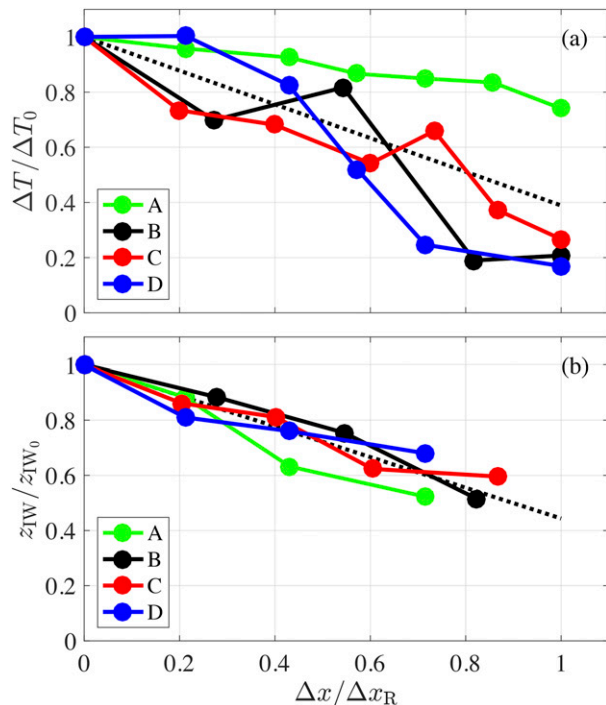


FIG. 15. NLIW events A–D (colored) (a) normalized temperature anomaly $\Delta T/\Delta T_0$ and (b) normalized z_{1W}/z_{1W_0} vs normalized upslope propagation distance $\Delta x/\Delta x_R$. The linear fit (dotted black) to events A–D in (a) has squared correlation $R^2 = 0.58$. The linear fit to all events in (b) has slope -0.56 (dotted black) and $R^2 = 0.89$. Note that z_{1W} is only estimated at locations with four thermistors in the vertical.

upslope propagation of broken internal solitary waves (e.g., Wallace and Wilkinson 1988; Helfrich 1992). Upslope event front temperature drop ΔT varied substantially (Fig. 14a). However, the normalized $\Delta T/\Delta T_0$ largely collapse as a linearly decaying function of $\Delta x/\Delta x_R$ (Fig. 15a) with best-fit slope -0.61 and squared correlation $R^2 = 0.58$. For events A–D, the dimensional z_{1W} upslope dependence was not as scattered as for ΔT (Fig. 14b). Similarly, the nondimensional z_{1W}/z_{1W_0} collapse very well as a linearly decaying function of $\Delta x/\Delta x_R$ (Fig. 15b) with best fit slope of -0.56 and $R^2 = 0.89$, again qualitatively consistent with laboratory studies (Wallace and Wilkinson 1988; Helfrich 1992; Marleau et al. 2014). The collapse of nondimensional ΔT and z_{1W} suggests the dynamics of the continuously stratified internal run-up into homogeneous water is largely self-similar.

Laboratory two-layer upslope gravity current deceleration is constant and depends upon g' , constant bed slope s , and the ratio h_i/h , where h_i represents gravity current height and h is the total water depth (Marleau et al. 2014). Adapting this scaling for

continuously stratified NLIW event deceleration results in

$$d_{gc} = \frac{1}{2} g'_0 s \frac{z_{1W_0}}{\tilde{h}_0} \left(1 - \frac{z_{1W_0}}{\tilde{h}_0} \right), \quad (12)$$

where g'_0 , z_{1W_0} , and \tilde{h}_0 are all at evaluated at x_0 . Here, the averaged bedslope from S8 to S4 is used ($s = 0.033$). The events A–D best-fit front speed at x_0 (c_{f0}) and the constant deceleration d_f [(11)] are compared to the two-layer gravity current scalings for speed c_{gc} [(10)] and upslope deceleration d_{gc} [(12)]. The events A–D c_{f0} varies from 0.04 to 0.08 m s^{-1} and is similar to the two-layer gravity current speed c_{gc} estimated at x_0 (Fig. 16a), although c_{gc} is generally larger than c_{f0} by more than a standard error (horizontal lines in Fig. 16a). The c_{f0} and c_{gc} fit has RMSE of 0.013 m s^{-1} and best-fit slope of 1.17. Events A–D d_f is very similar to d_{gc} (always within a standard error) over a large range (factor of 2.5) of deceleration (Fig. 16b). The d_f and d_{gc} fit has RMSE of $9 \times 10^{-7} \text{m s}^{-2}$ and best-fit slope of 0.84. The factor 2.5 variation in d_f is largely due to the ΔT_0 variations impacting g'_0 . The small error of the c_{f0} and d_f scalings indicates that for normally incident NLIW events propagating upslope into a homogeneous fluid, the two-layer gravity current scalings are appropriate.

Because both nondimensional ΔT and z_{1W} are largely self-similar with $\Delta x/\Delta x_R$, the upslope evolution of an offshore (at x_0) observed NLIW run-up event can be estimated knowing the total run-up distance Δx_R . At the onshore run-up limit Δx_R , the event front speed $c_f = dx_f/dt = 0$. With the quadratic front evolution, setting the derivative of (11) to zero and substituting yields

$$\Delta x_R = \frac{1}{2} \frac{c_{f0}^2}{d_f}. \quad (13)$$

The Δx_R estimated from (13) with c_{f0} and d_f reproduces the observed Δx_R defined in section 4a well (Fig. 17a), with RMSE of 13 m (less than the 18-m cross-shore resolution of the thermistor array, Fig. 1b) and a best-fit slope of 0.92 that is near unity. This demonstrates that with knowledge of offshore event front parameters (c_{f0} , d_f , ΔT_0 , and z_{1W_0}), the upslope distribution of these parameters can be well estimated.

However, event front observations from at least three locations along the axis of propagation are required to estimate c_{f0} and d_f and thus Δx_R via (13). The gravity current scalings for c_{gc} [(10)] and d_{gc} [(12)] only require vertical temperature coverage at a single location and can be used to estimate

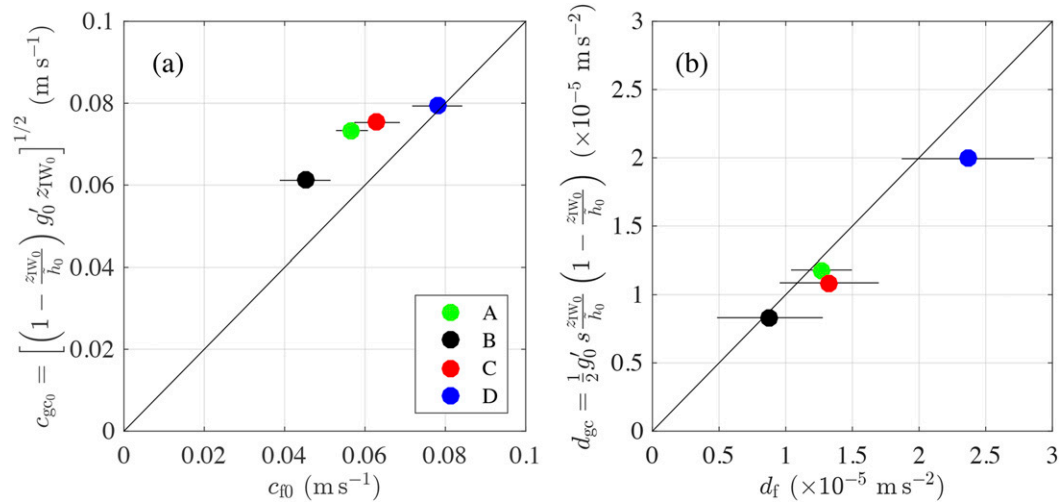


FIG. 16. (a) The best-fit gravity current speed c_{gc0} [(10)] vs NLIW front speed c_{f0} [(11)] at x_0 with RMSE of 0.013 m s^{-1} and best-fit slope 1.17. (b) Best-fit upslope gravity current deceleration d_{gc} [(12)] vs NLIW front deceleration d_f [(11)] with RMSE of $0.2 \times 10^{-5} \text{ m s}^{-2}$ and best-fit slope of 0.84. Both (a) and (b) are for events A–D. Horizontal black bars are the standard error in the best-fit values.

$$\Delta x_R = \frac{1}{2} \frac{c_{gc}^2}{d_{gc}}. \quad (14)$$

The gravity current scaling-based Δx_R [(14)] significantly overpredicts the observed Δx_R (Fig. 17b), with RMSE of 102 m and best-fit slope of 1.75. Relatively small errors in c_{gc} and d_{gc} (Fig. 16) cascade through (14) to generate these large errors. For example, with the best-fit slopes for c_{gc} (1.17) and d_{gc} (0.84) and the scaling (14), the predicted best-fit slope is 1.63, which is near the observed best-fit slope of 1.75 (Fig. 17b). This

demonstrates that predictions of total run-up distance Δx_R are very sensitive to small errors in run-up speed and deceleration.

5. Discussion

a. Internal run-up and comparison to laboratory and numerical studies

For the 14 events at S8, the event front speed is consistent with a internal gravity current (Fig. 11b) and the

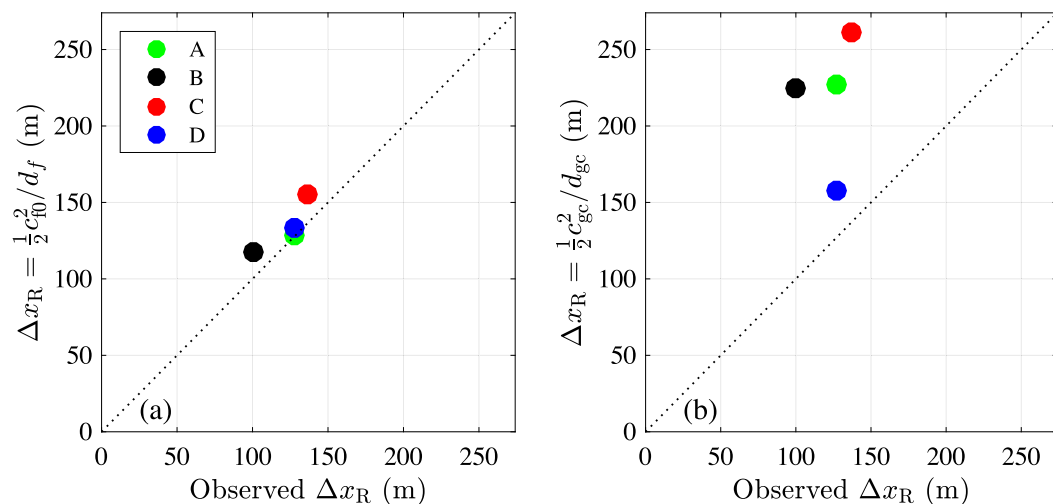


FIG. 17. Predicted NLIW event A–D (colored) propagation distance Δx_R vs observed Δx_R using (a) best fit front velocity c_{f0} at x_0 and deceleration d_f , and (b) two-layer gravity current velocity c_{gc} and deceleration d_{gc} . The RMSE is (a) 13 m and (b) 102 m.

ratio $|U'_b|/c_f$ is generally $O(1)$, suggesting that these events are internal bores (e.g., Pineda 1994; Moum et al. 2007; Walter et al. 2012; Nam and Send 2011). For the four isolated (A–D) events, the ratio $|U'_b|/c_f$ is also $O(1)$ (Table 1) and the upslope event evolution (speed and constant deceleration) is consistent both with upslope gravity currents (Marleau et al. 2014) and internal run-up of laboratory broken internal solitary waves (Helfrich 1992; Sutherland et al. 2013a). This all indicates that the internal wave breaking begins well offshore of S8 and that S8 and onshore locations are located within the internal swashzone where events propagate as bores, similar to the swashzone of a beach (e.g., Fiedler et al. 2015).

In a tidal estuary with a planar “internal beach,” Bourgault et al. (2007) observed cross-shore propagating and dissipating internal solitary waves of elevation from 25- to 10-m depth. In this dissipating region, the wave speed decreased linearly in the cross shore (dc_f/dx was constant). For the quadratic event front position [(11)], the event front speed as a function of x can be written as

$$c_f(x) = c_{f0} \left(1 - \frac{2d_f \Delta x}{c_{f0}^2} \right)^{1/2}, \quad (15)$$

which yields an approximately constant dc_f/dx for small $2d_f \Delta x/c_{f0}^2$. For the best-fit parameters, the event front dc_f/dx is approximately constant for about half of Δx_R . Thus, the upslope evolution of the internal run-up front speed is consistent with that of dissipating internal solitary waves Bourgault et al. (2007). However, the Bourgault et al. (2007) wave speeds were between 0.2 and 0.5 m s^{-1} , much faster than observed here because of the much stronger density gradients of the estuary setting than observed near the SIO pier.

The evolution of these continuously stratified dense bores propagating upslope into homogeneous fluid are consistent with two-layer upslope gravity current scalings (e.g., Fig. 16) using near-bed estimated ΔT and an interface height z_{IW} assuming equivalent potential energy [(5–8)]. From flat-bottom numerical simulations, a continuously stratified interface between upper and lower layers results in a weak decrease, relative to two-layer theory [(10)], of the gravity current speed c_{gc} (White and Helfrich 2014). With stratification similar to that observed in events A–D, the continuously stratified model suggests the c_{gc} found from (10) should be reduced by $\approx 5\%$ (White and Helfrich 2014). This indicates that applying the two-layer approximation to these continuously stratified internal run-up events is appropriate and also may account for some of the c_{gc} bias error (Fig. 11b).

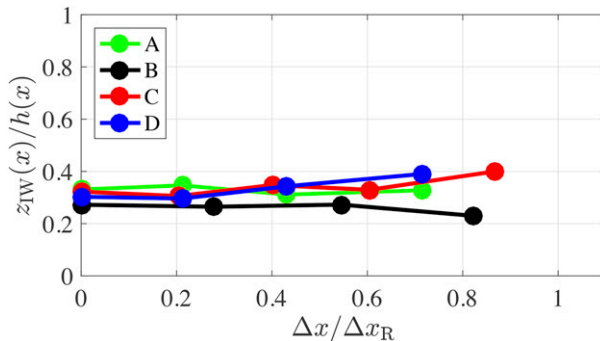


FIG. 18. NLIW events A–D (colored) normalized z_{IW}/h vs upslope propagation distance $\Delta x/\Delta x_R$.

The constant upslope two-layer gravity current deceleration can be derived by assuming a weak slope such that at all locations the front speed follows the Shin et al. (2004) gravity current speed [(10)] with constant Froude number F_0 that depends on $\delta = z_{IW}/h$ (Sutherland et al. 2013b; Marleau et al. 2014). The quadratic in time dependence of the front position is derived with $h(x) = -sx$. This requires that $\delta = z_{IW}/h$ be constant upslope. For the four isolated events A–D, $z_{IW}/h \approx 0.3$ at $\Delta x/\Delta x_R = 0$ and does not vary by more than ± 0.1 all the way to $\Delta x/\Delta x_R = 1$ (Fig. 18). The linear upslope reduction in z_{IW}/z_{IW_0} with $\Delta x/\Delta x_R$ is qualitatively consistent with the observed linear upslope amplitude decay of a dissipating internal solitary wave on a linear slope (Bourgault et al. 2007). Linear upslope z_{IW}/z_{IW_0} reduction is also consistent with laboratory internal solitary wave run-up for all incident wave amplitudes (Wallace and Wilkinson 1988; Helfrich 1992), and with laboratory observations of a two-layer upslope gravity current on shallow slopes (Marleau et al. 2014). This all supports the assumption that such internal bores are self-similar (Wallace and Wilkinson 1988). Note, however, that in laboratory internal solitary wave experiments, the origin ($\Delta x = 0$) is the location where solitary wave breaking is initiated (breakpoint), which would be offshore of S8, and unlike two layer systems, here ΔT is not constant in the upslope direction, resulting in g' variations.

The observed linearly decaying self-similar $\Delta T/\Delta T_0$ decrease with $\Delta x/\Delta x_R$ is also qualitatively consistent with two-layer laboratory upslope normalized density decay (Wallace and Wilkinson 1988), although again the origin is relative to the internal solitary wave breakpoint. The two-layer laboratory density decay also contained significantly more scatter than did normalized height (Wallace and Wilkinson 1988), again consistent with these observations (Fig. 15). Upslope laboratory $\Delta T/\Delta T_0$ decrease with $\Delta x/\Delta x_R$ was attributed to mixing and

entrainment from the surrounding fluid and downrush from previous events. For the continuously stratified events A–D, the reduction in ΔT may also be due to mixing at the event front. Prior to the event start, the temperature was homogeneous. With the event arrival, the S8 onshore near-bed and offshore near-surface flow and the delayed near-surface cooling (Fig. 8) also suggest mixing in the event front, as the offshore-flowing near-surface water would remain warm otherwise. However, the observed ΔT reduction may also be because upslope locations are closer to the surface (higher z), and S8 temperature drop is reduced at higher z (Fig. 8). Some combination of these two mechanisms may explain the upslope ΔT decrease.

b. Potential vertical mixing during the NLIW rundown

Any mixing at the event front cannot be quantified here. However, after internal run-up reaches x_R , dense water then flows back downslope (rundown), during which significant mixing occurs in both observations in $h \approx 15$ m (Walter et al. 2012) and numerical simulations (Arthur and Fringer 2014). Here, vertical mixing in the internal swashzone during the rundown of example event C (temperature in Fig. 8a) is inferred through the evolution of vertically integrated and horizontally averaged potential energy $\Delta\langle\text{PE}\rangle$, buoyancy frequency squared N^2 , shear-squared S^2 , and gradient Richardson number $\text{Ri} = N^2/S^2$ that indicates when a stratified flow is dynamically unstable (<0.25).

The time evolution of potential energy [(5)] is horizontally averaged over the wave run-up extent

$$\langle\text{PE}\rangle(t) = \Delta x_R^{-1} \int_{\text{S8}}^{x_R} \text{PE}(x, t) dx, \quad (16)$$

and the change in this quantity from the event arrival at t_{f1} is

$$\Delta\langle\text{PE}\rangle(t) = \langle\text{PE}\rangle(t) - \langle\text{PE}\rangle(t_{f1}), \quad (17)$$

which evolves because of both reversible (adiabatic advection) and irreversible (mixing) density changes (e.g., Winters et al. 1995). The stratification is given by $N^2 = (g/\rho_0)\partial\rho(z)/\partial z$, where $\partial\rho/\partial z$ is found from a least squares fit over a mid-depth range at S8 ($-5.7 \leq z \leq -2.7$ m). Baroclinic velocity shear-squared $S^2 = (\Delta U'/\Delta z)^2 + (\Delta V'/\Delta z)^2$ is found for the same middepth range. Here, $\Delta U'$ (and $\Delta V'$) is the difference between the vertically averaged baroclinic velocity near the top of the middepth range ($-4.2 \leq z \leq -2.7$ m) and near the bottom of the middepth range ($-5.7 \leq z \leq -4.2$ m). The vertical distance between the centers of the two ranges $\Delta z = 1.5$ m.

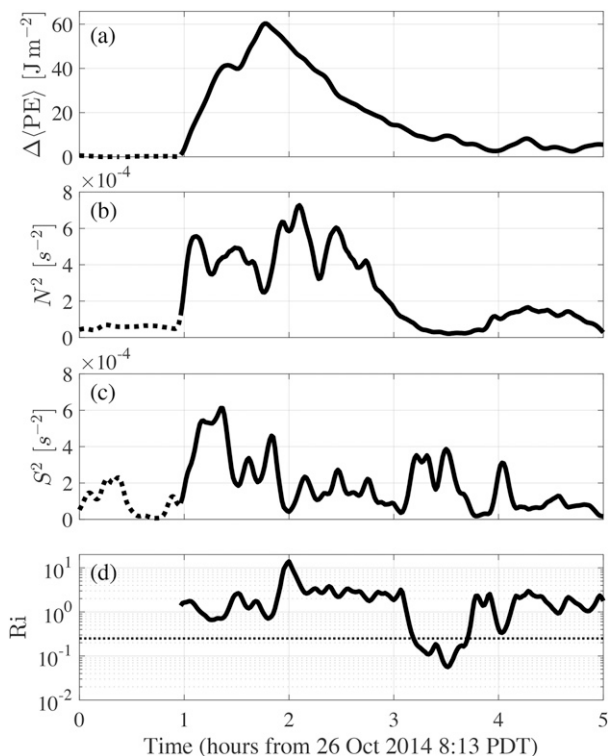


FIG. 19. Five-hour time series during event C of (a) event-induced change in horizontally averaged potential energy $\Delta\langle\text{PE}\rangle$ [(17)], (b) midwater squared buoyancy frequency N^2 at S8, (c) squared midwater shear S^2 at S8, and (d) the gradient Richardson number $\text{Ri} = N^2/S^2$ at S8. All values have been smoothed (5-min filter). Dotted lines in (a)–(c) indicate measurements recorded before the arrival of the event front at hour 1. The horizontal dotted line in (d) is the critical Richardson value (0.25).

Before the event arrival, $\Delta\langle\text{PE}\rangle$, N^2 , and S^2 were consistent and low (dotted lines, Figs. 19a–c). After the event onset near hour 1, cold water pulsed onshore, elevating $\Delta\langle\text{PE}\rangle$ to near 60 J m^{-2} approximately 45 min later (Fig. 19a). The cold pulse stratified the water column while creating shear at middepths, leading to N^2 and S^2 above $4 \times 10^{-4} \text{ s}^{-2}$ (Figs. 19b,c). During the onrush (hour 1 to 2 when near-bottom U' was positive; Fig. 8b), Ri was near 1, though always above 0.25, suggesting that sustained local vertical mixing at S8 was unlikely (Fig. 19d), consistent with model studies and microstructure observations on shallow slopes (e.g., Moore et al. 2016; Bourgault et al. 2008). Although these observations show no evidence of shear-driven mixing during the onrush, observations of similar bores have measured elevated turbulence (both advected and locally generated) during the bore passage very near the bottom (Richards et al. 2013). Between hours 2 and 3, near-bed U' is offshore as cold water begins to advect back downslope (Fig. 8b).

As S8 bottom temperature increases (Fig. 8a), $\Delta\langle\text{PE}\rangle$ and N^2 decrease (Figs. 19a,b). However, Ri is consistently above the critical value (Fig. 19d), indicating that local shear-driven midwater vertical mixing is still unlikely at S8.

As the rundown intensifies after hour 3 at S8, midwater S^2 at S8 increases again while N^2 is small, causing Ri to drop below the critical value (Figs. 19b–d). At this time, shear-driven mixing at middepths is possible at S8. The timing of this drop in Ri corresponds with a period of bottom warming and surface cooling (Fig. 8a), with the transition depth between the cooling surface and warming bottom near where U' changes sign ($x \approx -3.5$ m). The direction of U' at this time (onshore at the surface and offshore at depth) potentially advects recently mixed cooler water near the surface offshore of S8 onshore. The difference in local mixing at S8 between internal run-up uprush and downrush is consistent with differences in mixing and sediment suspension during uprush and downrush in a surface gravity swashzone (Puleo et al. 2000).

After the event (4–5 h), the internal swashzone is slightly cooler (cf. cross-shore bottom temperature before and after the event at locations offshore of x_R in Fig. 9a and vertical temperature structure at S8 in Fig. 8a). Because of the postevent remaining cold water, $\Delta\langle\text{PE}\rangle \approx 4.9 \text{ J m}^{-2}$, which is roughly 10% the maximum $\Delta\langle\text{PE}\rangle$. As the sun was warming the nearshore at this time (decreasing $\Delta\langle\text{PE}\rangle$) and alongshore currents were small (mean $\bar{V} < 0.003 \text{ m s}^{-1}$), the residual $\Delta\langle\text{PE}\rangle$ is likely due to irreversible mixing during the event. This residual $\Delta\langle\text{PE}\rangle$ implies an average irreversible buoyancy flux of $5 \times 10^{-4} \text{ W m}^{-2}$, which is nearly a factor 50 lower than that inferred from highly stratified estuary observations (Bourgault et al. 2007).

c. Complexity of NLIW run-up in the internal swashzone

For the four isolated events, the upslope evolution of event parameters [$c_f(x)$, $\Delta T(x)$, $z_{\text{TW}}(x)$] can be predicted (although Δx_R is overpredicted) given water column observations at some offshore location within the internal swashzone. This can provide insight into the onshore transport of intertidal settling larvae (e.g., Pineda 1999) and other tracers exchanged with the surfzone. However, these four events were relatively simple (isolated, normally incident, and homogeneous pre-event), analogous to laboratory observations. Even the 14 events at S8 (Figs. 10, 11b) were relatively simple. These restrictions on event and isolated event definitions eliminated most period I NLIW cold pulses and several significant events from period II (e.g., Figs. 3, 4).

In general, the NLIW field is very complex, containing large-amplitude isotherm oscillations over a range of frequencies (M_2 , its harmonics, as well above 1 cph) that evolve over spring-neap conditions. The broad S18 high-frequency spectral peak (centered between 6–10 cph) observed during period I (red, Fig. 7c) is also present in other studies, particularly near topographic features (e.g., Desaubies 1975; D'Asaro et al. 2007). Overlapping cold pulses at variable angles of incidence and potential reflection (e.g., Fig. 12) are common. This region onshore of a submarine canyon system (Fig. 1a) may also be unusual in terms of the NLIW field. The observed complex NLIW conditions demonstrate that the internal swashzone is more complex than that described only from isolated events, similar to a surface gravity wave swashzone.

The wave-by-wave evolution of internal run-up is likely affected by interaction between individual run-up events. Run-up events can interact via bore-bore capture (potentially observed in Fig. 12), which in a surface gravity swashzone leads to the largest run-up events (e.g., García-Medina et al. 2017). Event interactions also can include modification of background conditions through which subsequent waves propagate, or interference between the previous event rundown and run-up of the next event (e.g., Moore et al. 2016; Davis et al. 2017, manuscript submitted to *Geophys. Res. Lett.*). Laboratory observations indicate internal wave breaking and elevated mixing due to interaction with a previous event's downrush (Wallace and Wilkinson 1988; Helfrich 1992). Downslope bottom flow prior to the event (e.g., Helfrich 1992; Sutherland et al. 2013a) was occasionally observed (e.g., hour 1.75 below $z = -6$ m in Fig. 8b). Although not observed here, the downrush may eventually detach, similar to laboratory observations of gravity current intrusions (Maurer et al. 2010). Internal bores have been previously observed to resuspend fine sediments creating an intermediate layer offshore (Masunaga et al. 2015). While the location of maximum sediment suspension is likely offshore of the study area (Bourgault et al. 2014), currents from the nearshore downrush may contribute to sediment redistribution and the formation of intermediate nepheloid layers similar to those observed from internal wave reflection (e.g., McPhee-Shaw and Kunze 2002).

Statistics of the offshore surface gravity wave field can be related to statistics of run-up extent for a surface gravity swashzone (e.g., Holland and Holman 1993; Raubenheimer and Guza 1996). For example, offshore significant wave height, peak period, and beach slope can be used to reasonably accurately simulate the cross-shore variance of run-up excursion up a beach (e.g., Stockdon et al. 2006; Senechal et al. 2011). In less

complicated locations (with a predictable internal wave climate), offshore internal tide and stratification statistics potentially can be combined with beach slope information to parameterize internal run-up statistics.

6. Summary

For 30 days between 29 September and 29 October 2014, a dense thermistor array sampled temperature in depths shallower than 18 m, and a bottom-mounted ADCP in 8-m depth sampled 1-min-averaged velocity in 0.5-m vertical bins. A rich and variable internal wave field was observed from 18-m depth to the shoreline, with isotherm oscillations at a variety of periods, and a high-frequency spectral peak (near 10-min periods) when stratification was strong. Isotherm excursions were regularly ± 6 m during periods of high stratification; though isotherm excursions were less extreme, variability at all frequencies was reduced, and no high-frequency spectral peak was observed when stratification decreased.

Cross-shore coherent pulses of cold water at M_2 and M_4 time scales were regularly observed throughout the observational period. NLIW event (rapid temperature drops and recovery) is evident from the baroclinic transport of cold water upslope, occasionally causing temperature drops of 0.7°C in 5 min in water as shallow as 2 m. Fourteen isolated NLIW events were observed in 8-m depth propagating upslope with speeds c_f ranging from 1.4 to 7.4 cm s^{-1} , propagation angles θ from -5° to 23° and temperature drops ΔT between 0.3° and 1.7°C , decreasing upslope. The two-layer equivalent gravity current height z_{IW} decreased linearly upslope from initial values between 2.1 and 2.5 m in 8-m depth and was consistent with observations of baroclinic velocity. Baroclinic bottom current during the upslope event propagation ($|U'_b|$) was near the event front propagation speed, indicating high nonlinearity, with mean $|U'_b|/c_f = 0.7$.

The upslope evolution of ΔT , z_{IW} , and c_f for four representative events most similar to two-layer laboratory conditions (alongshore uniform, shore-normal, isolated, and propagating into homogeneous fluid) are qualitatively consistent with laboratory observations of broken internal wave run-up. Normalized ΔT and z_{IW} for these events collapse as a linearly decaying function of normalized run-up distance, and upslope gravity current scalings described the front speed c_{f0} and deceleration d_f well. The associated total run-up distance Δx_R was also well predicted from c_{f0} and d_f , with RMSE less than the resolution of the cross-shore thermistor array. However, Δx_R prediction with gravity current scalings has significant error because of sensitivity to c_{f0} .

Depressed temperature remained in the nearshore region for hours, until receding back downslope. Bottom temperature warmed and surface temperatures cooled during the receding rundown of an example event. The gradient Richardson number remained below the critical value (0.25) at this time, indicating shear-driven mixing was occurring consistent with laboratory and modeling studies. The four NLIW events selected to compare with laboratory studies are simple cases. In general, NLIW run-up is more complicated because of superposition (in ways similar to bore-bore capture) interaction with previous (receding) events, or as the diverse offshore NLIW field evolves. Any understanding of the internal swashzone beyond the most simple cases may require descriptions of complex interactions or a statistical approach similar to those used to describe the surface gravity wave swashzone.

Acknowledgments. This publication was prepared under NOAA Grant NA14OAR4170075/ECKMAN, California Sea Grant College Program Project R/HCME-26, through NOAA's National Sea Grant College Program, U.S. Dept. of Commerce. The statements, findings, conclusions, and recommendations are those of the authors and do not necessarily reflect the views of California Sea Grant, NOAA, or the U.S. Dept. of Commerce. Additional support for F. Feddersen was provided by the National Science Foundation, and the Office of Naval Research. B. Woodward, B. Boyd, K. Smith, R. Grenzeback, R. Walsh, J. MacKinnon, A. Waterhouse, M. Hamann, and many volunteer scientific divers assisted with field work. Supplemental data were supplied by NOAA, CDIP, SCCOOS, and CORDC with help from C. Olfe, B. O'Reilly, and M. Otero. D. Grimes, S. Suanda, and two anonymous reviewers provided feedback that significantly improved the manuscript.

REFERENCES

- Alberdy, M. S., S. Billheimer, M. M. Hamann, C. Y. Ou, V. Tamsitt, A. J. Lucas, and M. H. Alford, 2017: A reflecting, steepening, and breaking internal tide in a submarine canyon. *J. Geophys. Res. Oceans*, **122**, 6872–6882, <https://doi.org/10.1002/2016JC012583>.
- Arthur, R. S., and O. B. Fringer, 2014: The dynamics of breaking internal solitary waves on slopes. *J. Fluid Mech.*, **761**, 360–398, <https://doi.org/10.1017/jfm.2014.641>.
- , and —, 2016: Transport by breaking internal gravity waves on slopes. *J. Fluid Mech.*, **789**, 93–126, <https://doi.org/10.1017/jfm.2015.723>.
- Bourgault, D., M. D. Blokhina, R. Mirshak, and D. E. Kelley, 2007: Evolution of a shoaling internal solitary wavetrain. *Geophys. Res. Lett.*, **34**, L03601, <https://doi.org/10.1029/2006GL028462>.

- , D. E. Kelley, and P. S. Galbraith, 2008: Turbulence and boluses on an internal beach. *J. Mar. Res.*, **66**, 563–588, <https://doi.org/10.1357/002224008787536835>.
- , D. C. Janes, and P. S. Galbraith, 2011: Observations of a large-amplitude internal wave train and its reflection off a steep slope. *J. Phys. Oceanogr.*, **41**, 586–600, <https://doi.org/10.1175/2010JPO4464.1>.
- , M. Morsilli, C. Richards, U. Neumeier, and D. Kelley, 2014: Sediment resuspension and nepheloid layers induced by long internal solitary waves shoaling orthogonally on uniform slopes. *Cont. Shelf Res.*, **72**, 21–33, <https://doi.org/10.1016/j.csr.2013.10.019>.
- D'Asaro, E. A., R.-C. Lien, and F. Henyey, 2007: High-frequency internal waves on the Oregon continental shelf. *J. Phys. Oceanogr.*, **37**, 1956–1967, <https://doi.org/10.1175/JPO3096.1>.
- Desaubies, Y. J. F., 1975: A linear theory of internal wave spectra and coherences near the Väisälä frequency. *J. Geophys. Res.*, **80**, 895–899, <https://doi.org/10.1029/JC080i006p00895>.
- Fiedler, J. W., K. L. Brodie, J. E. McNinch, and R. T. Guza, 2015: Observations of runup and energy flux on a low-slope beach with high-energy, long-period ocean swell. *Geophys. Res. Lett.*, **42**, 9933–9941, <https://doi.org/10.1002/2015GL066124>.
- García-Medina, G., H. T. Özkan-Haller, R. A. Holman, and P. Ruggiero, 2017: Large runup controls on a gently sloping dissipative beach. *J. Geophys. Res. Oceans*, **122**, 5998–6010, <https://doi.org/10.1002/2017JC012862>.
- Garrett, C., and E. Kunze, 2007: Internal tide generation in the deep ocean. *Annu. Rev. Fluid Mech.*, **39**, 57–87, <https://doi.org/10.1146/annurev.fluid.39.050905.110227>.
- Helfrich, K. R., 1992: Internal solitary wave breaking and runup on a uniform slope. *J. Fluid Mech.*, **243**, 133–154, <https://doi.org/10.1017/S0022112092002660>.
- Holland, K. T., and R. A. Holman, 1993: The statistical distribution of swash maxima on natural beaches. *J. Geophys. Res.*, **98**, 10 271–10 278, <https://doi.org/10.1029/93JC00035>.
- Holloway, P. E., E. Pelinovsky, and T. Talipova, 1999: A generalized Korteweg-de Vries model of internal tide transformation in the coastal zone. *J. Geophys. Res.*, **104**, 18 333–18 350, <https://doi.org/10.1029/1999JC900144>.
- Inman, D., C. Nordstrom, and R. Flick, 1976: Currents in submarine canyons: An air-sea-land interaction. *Annu. Rev. Fluid Mech.*, **8**, 275–310, <https://doi.org/10.1146/annurev.fl.08.010176.001423>.
- Jaffe, J. S., P. J. S. Franks, P. L. D. Roberts, D. Mirza, C. Schurgers, R. Kastner, and A. Boch, 2017: A swarm of autonomous miniature underwater robot drifters for exploring submesoscale ocean dynamics. *Nat. Commun.*, **8**, 14189, <https://doi.org/10.1038/ncomms14189>.
- Leichter, J., S. Wing, S. Miller, and M. Denny, 1996: Pulsed delivery of subthermocline water to conch reef (Florida Keys) by internal tidal bores. *Limnol. Oceanogr.*, **41**, 1490–1501, <https://doi.org/10.4319/lo.1996.41.7.1490>.
- Lennert-Cody, C. E., and P. J. Franks, 1999: Plankton patchiness in high-frequency internal waves. *Mar. Ecol. Prog. Ser.*, **186**, 59–66, <https://doi.org/10.3354/meps186059>.
- Lilly, J. M., 2016: jlab: A data analysis package for Matlab, version 1.6.2. Accessed 31 January 2018, <http://www.jmlilly.net/jmlsoft.html>.
- Lucas, A., C. Dupont, V. Tai, J. L. Largier, B. Palenik, and P. J. Franks, 2011a: The green ribbon: Multiscale physical control of phytoplankton productivity and community structure over a narrow continental shelf. *Limnol. Oceanogr.*, **56**, 611–626, <https://doi.org/10.4319/lo.2011.56.2.0611>.
- , P. Franks, and C. Dupont, 2011b: Horizontal internal-tide fluxes support elevated phytoplankton productivity over the inner continental shelf. *Limnol. Oceanogr. Fluids Environ.*, **1**, 56–74, <https://doi.org/10.1215/21573698-1258185>.
- MacKinnon, J. A., and M. C. Gregg, 2005: Spring mixing: Turbulence and internal waves during restratification on the New England shelf. *J. Phys. Oceanogr.*, **35**, 2425–2443, <https://doi.org/10.1175/JPO2821.1>.
- Marino, B., L. Thomas, and P. Linden, 2005: The front condition for gravity currents. *J. Fluid Mech.*, **536**, 49–78, <https://doi.org/10.1017/S0022112005004933>.
- Marleau, L. J., M. R. Flynn, and B. R. Sutherland, 2014: Gravity currents propagating up a slope. *Phys. Fluids*, **26**, 046605, <https://doi.org/10.1063/1.4872222>.
- Masunaga, E., H. Homma, H. Yamazaki, O. B. Fringer, T. Nagai, Y. Kitade, and A. Okayasu, 2015: Mixing and sediment resuspension associated with internal bores in a shallow bay. *Cont. Shelf Res.*, **110**, 85–99, <https://doi.org/10.1016/j.csr.2015.09.022>.
- Maurer, B. D., D. T. Bolster, and P. F. Linden, 2010: Intrusive gravity currents between two stably stratified fluids. *J. Fluid Mech.*, **647**, 53–69, <https://doi.org/10.1017/S0022112009993752>.
- McPhee-Shaw, E. E., and E. Kunze, 2002: Boundary layer intrusions from a sloping bottom: A mechanism for generating intermediate nepheloid layers. *J. Geophys. Res.*, **107**, 3050, <https://doi.org/10.1029/2001JC000801>.
- Moore, C. D., J. R. Koseff, and E. L. Hult, 2016: Characteristics of bolus formation and propagation from breaking internal waves on shelf slopes. *J. Fluid Mech.*, **791**, 260–283, <https://doi.org/10.1017/jfm.2016.58>.
- Moum, J. N., D. Farmer, W. Smyth, L. Armi, and S. Vagle, 2003: Structure and generation of turbulence at interfaces strained by internal solitary waves propagating shoreward over the continental shelf. *J. Phys. Oceanogr.*, **33**, 2093–2112, [https://doi.org/10.1175/1520-0485\(2003\)033<2093:SAGOTA>2.0.CO;2](https://doi.org/10.1175/1520-0485(2003)033<2093:SAGOTA>2.0.CO;2).
- , J. M. Klymak, J. D. Nash, A. Perlin, and W. D. Smyth, 2007: Energy transport by nonlinear internal waves. *J. Phys. Oceanogr.*, **37**, 1968–1988, <https://doi.org/10.1175/JPO3094.1>.
- Nam, S., and U. Send, 2011: Direct evidence of deep water intrusions onto the continental shelf via surging internal tides. *J. Geophys. Res.*, **116**, C05004, <https://doi.org/10.1029/2010JC006692>.
- Nash, J. D., S. M. Kelly, E. L. Shroyer, J. N. Moum, and T. F. Duda, 2012: The unpredictable nature of internal tides on continental shelves. *J. Phys. Oceanogr.*, **42**, 1981–2000, <https://doi.org/10.1175/JPO-D-12-028.1>.
- O'Reilly, W., and R. Guza, 1991: Comparison of spectral refraction and refraction-diffraction wave models. *J. Waterw. Port Coastal Ocean Eng.*, **117**, 199–215, [https://doi.org/10.1061/\(ASCE\)0733-950X\(1991\)117:3\(199\)](https://doi.org/10.1061/(ASCE)0733-950X(1991)117:3(199)).
- , and —, 1998: Assimilating coastal wave observations in regional swell predictions. Part I: Inverse methods. *J. Phys. Oceanogr.*, **28**, 679–691, [https://doi.org/10.1175/1520-0485\(1998\)028<0679:ACWOIR>2.0.CO;2](https://doi.org/10.1175/1520-0485(1998)028<0679:ACWOIR>2.0.CO;2).
- Omand, M. M., J. J. Leichter, P. J. S. Franks, A. J. Lucas, R. T. Guza, and F. Feddersen, 2011: Physical and biological processes underlying the sudden appearance of a red-tide surface patch in the nearshore. *Limnol. Oceanogr.*, **56**, 787–801, <https://doi.org/10.4319/lo.2011.56.3.0787>.
- , F. Feddersen, P. J. S. Franks, and R. T. Guza, 2012: Episodic vertical nutrient fluxes and nearshore phytoplankton blooms in Southern California. *Limnol. Oceanogr.*, **57**, 1673–1688, <https://doi.org/10.4319/lo.2012.57.6.1673>.

- Pineda, J., 1991: Predictable upwelling and the shoreward transport of planktonic larvae by internal tidal bores. *Science*, **253**, 548–551, <https://doi.org/10.1126/science.253.5019.548>.
- , 1994: Internal tidal bores in the nearshore: Warm-water fronts, seaward gravity currents and the onshore transport of neustonic larvae. *J. Mar. Res.*, **52**, 427–458, <https://doi.org/10.1357/0022240943077046>.
- , 1999: Circulation and larval distribution in internal tidal bore warm fronts. *Limnol. Oceanogr.*, **44**, 1400–1414, <https://doi.org/10.4319/lo.1999.44.6.1400>.
- Puleo, J. A., R. A. Beach, R. A. Holman, and J. S. Allen, 2000: Swash zone sediment suspension and transport and the importance of bore-generated turbulence. *J. Geophys. Res.*, **105**, 17 021–17 044, <https://doi.org/10.1029/2000JC900024>.
- Quaresma, L. S., J. Vitorino, A. Oliveira, and J. da Silva, 2007: Evidence of sediment resuspension by nonlinear internal waves on the western Portuguese mid-shelf. *Mar. Geol.*, **246**, 123–143, <https://doi.org/10.1016/j.margeo.2007.04.019>.
- Raubenheimer, B., and R. T. Guza, 1996: Observations and predictions of runup. *J. Geophys. Res.*, **101**, 25 575–25 587, <https://doi.org/10.1029/96JC02432>.
- Richards, C., D. Bourgault, P. S. Galbraith, A. Hay, and D. E. Kelley, 2013: Measurements of shoaling internal waves and turbulence in an estuary. *J. Geophys. Res. Oceans*, **118**, 273–286, <https://doi.org/10.1029/2012JC008154>.
- Senechal, N., G. Coco, K. R. Bryan, and R. A. Holman, 2011: Wave runup during extreme storm conditions. *J. Geophys. Res.*, **116**, C07032, <https://doi.org/10.1029/2010JC006819>.
- Shepard, F., N. Marshall, and P. McLoughlin, 1974: Currents in submarine canyons. *Deep-Sea Res. Oceanogr. Abstr.*, **21**, 691–706, [https://doi.org/10.1016/0011-7471\(74\)90077-1](https://doi.org/10.1016/0011-7471(74)90077-1).
- Shin, J. O., S. B. Dalziel, and P. Linden, 2004: Gravity currents produced by lock exchange. *J. Fluid Mech.*, **521**, 1–34, <https://doi.org/10.1017/S002211200400165X>.
- Shroyer, E., J. Moum, and J. Nash, 2011: Nonlinear internal waves over New Jersey's continental shelf. *J. Geophys. Res.*, **116**, C03022, doi:10.1029/2010JC006332.
- Sinnett, G., and F. Feddersen, 2014: The surf zone heat budget: The effect of wave heating. *Geophys. Res. Lett.*, **41**, 7217–7226, <https://doi.org/10.1002/2014GL061398>.
- , and —, 2016: Observations and parameterizations of surf-zone albedo. *Methods Oceanogr.*, **17**, 319–334, <https://doi.org/10.1016/j.mio.2016.07.001>.
- Stanton, T. P., and L. A. Ostrovsky, 1998: Observations of highly nonlinear internal solitons over the continental shelf. *Geophys. Res. Lett.*, **25**, 2695–2698, <https://doi.org/10.1029/98GL01772>.
- Stockdon, H. F., R. A. Holman, P. A. Howd, and A. H. Sallenger, 2006: Empirical parameterization of setup, swash, and runup. *Coast. Eng.*, **53**, 573–588, <https://doi.org/10.1016/j.coastaleng.2005.12.005>.
- Suanda, S. H., and J. A. Barth, 2015: Semidiurnal baroclinic tides on the central Oregon inner shelf. *J. Phys. Oceanogr.*, **45**, 2640–2659, <https://doi.org/10.1175/JPO-D-14-0198.1>.
- Sutherland, B., K. Barrett, and G. Ivey, 2013a: Shoaling internal solitary waves. *J. Geophys. Res. Oceans*, **118**, 4111–4124, <https://doi.org/10.1002/jgrc.20291>.
- Sutherland, B. R., D. Polet, and M. Campbell, 2013b: Gravity currents shoaling on a slope. *Phys. Fluids*, **25**, 086604, <https://doi.org/10.1063/1.4818440>.
- Thomson, D. J., 1982: Spectrum estimation and harmonic analysis. *Proc. IEEE*, **70**, 1055–1096, <https://doi.org/10.1109/PROC.1982.12433>.
- Thorpe, S., 1999: The generation of alongslope currents by breaking internal waves. *J. Phys. Oceanogr.*, **29**, 29–38, [https://doi.org/10.1175/1520-0485\(1999\)029<0029:TGOACB>2.0.CO;2](https://doi.org/10.1175/1520-0485(1999)029<0029:TGOACB>2.0.CO;2).
- Wallace, B., and D. Wilkinson, 1988: Runup of internal waves on a gentle slope in a two-layered system. *J. Fluid Mech.*, **191**, 419–442, <https://doi.org/10.1017/S0022112088001636>.
- Walter, R. K., C. B. Woodson, R. S. Arthur, O. B. Fringer, and S. G. Monismith, 2012: Nearshore internal bores and turbulent mixing in southern Monterey Bay. *J. Geophys. Res.*, **117**, C07017, <https://doi.org/10.1029/2012JC008115>.
- , —, P. R. Leary, and S. G. Monismith, 2014: Connecting wind-driven upwelling and offshore stratification to nearshore internal bores and oxygen variability. *J. Geophys. Res. Oceans*, **119**, 3517–3534, <https://doi.org/10.1002/2014JC009998>.
- , M. Stastna, C. B. Woodson, and S. G. Monismith, 2016: Observations of nonlinear internal waves at a persistent coastal upwelling front. *Cont. Shelf Res.*, **117**, 100–117, <https://doi.org/10.1016/j.csr.2016.02.007>.
- White, B. L., and K. R. Helfrich, 2014: A model for internal bores in continuous stratification. *J. Fluid Mech.*, **761**, 282–304, <https://doi.org/10.1017/jfm.2014.599>.
- Winant, C. D., 1974: Internal surges in coastal waters. *J. Geophys. Res.*, **79**, 4523–4526, <https://doi.org/10.1029/JC079i030p04523>.
- , and A. W. Bratkovich, 1981: Temperature and currents on the Southern California shelf: A description of the variability. *J. Phys. Oceanogr.*, **11**, 71–86, [https://doi.org/10.1175/1520-0485\(1981\)011<0071:TACOTS>2.0.CO;2](https://doi.org/10.1175/1520-0485(1981)011<0071:TACOTS>2.0.CO;2).
- Winters, K. B., P. N. Lombard, J. J. Riley, and E. A. D'Asaro, 1995: Available potential energy and mixing in density-stratified fluids. *J. Fluid Mech.*, **289**, 115–128, <https://doi.org/10.1017/S002211209500125X>.
- Wong, S. H. C., A. E. Santoro, N. J. Nidzieko, J. L. Hench, and A. B. Boehm, 2012: Coupled physical, chemical, and microbiological measurements suggest a connection between internal waves and surf zone water quality in the Southern California Bight. *Cont. Shelf Res.*, **34**, 64–78, <https://doi.org/10.1016/j.csr.2011.12.005>.
- Wunsch, C., 1996: *The Ocean Circulation Inverse Problem*. Cambridge University Press, 458 pp., <https://doi.org/10.1017/CBO9780511629570>.
- Zhang, S., M. H. Alford, and J. B. Mickett, 2015: Characteristics, generation and mass transport of nonlinear internal waves on the Washington continental shelf. *J. Geophys. Res. Oceans*, **120**, 741–758, <https://doi.org/10.1002/2014JC010393>.